Superparamagnetic iron-oxide based nanoparticles for the separation and recovery of precious metals from solution

Eugene Marlin Lakay

A thesis submitted to the

University of Stellenbosch

in fulfillment of the requirements for the degree of

Master of Science

Supervisor: Professor Klaus R. Koch   **March 2009**

_____

1.2.1 Crystal structure of iron oxide based nanoparticles - magnetite

Among all iron oxide nanoparticles, magnetite (Fe_3O_4) presents the most interesting properties due to its unique magnetic structure as a result of the presence of iron cations in two valence states, Fe^{2+} and Fe^{3+} in the crystal structure. For that reason, only magnetite and related materials was studied. Magnetite is found in abundance in nature and can also be readily synthesized.[42,63]

Magnetite is a cubic mineral with an inverse spinel structure as shown in *Figure 1*. The inverse spinel structure of magnetite has the general formula $Fe_3O_4 = (Fe^{3+})_A (Fe^{3+}Fe^{2+})_B O_4$, where A and B symbolize the iron cations which are distributed on tetrahedral and octahedral interstitial sites, respectively. The Fe^{2+} ions and half the Fe^{3+} ions occupy octahedral sites; the other half of the Fe^{3+} ions occupies tetrahedral sites. As illustrated in *Figure 1*, a unit cell consists of four A and four B sites with lattice constants of a = 8.396 Å. The three-fold axis of rotation is along the diagonal [111] of the cubic cell. The inverse spinel structure of Fe_3O_4 consists of oxide ions in a face-centered cubic (fcc) close packed arrangement in which 1/3 of tetrahedral interstices and 2/3 of octahedral interstices coordinate with oxide ions.[42,63]
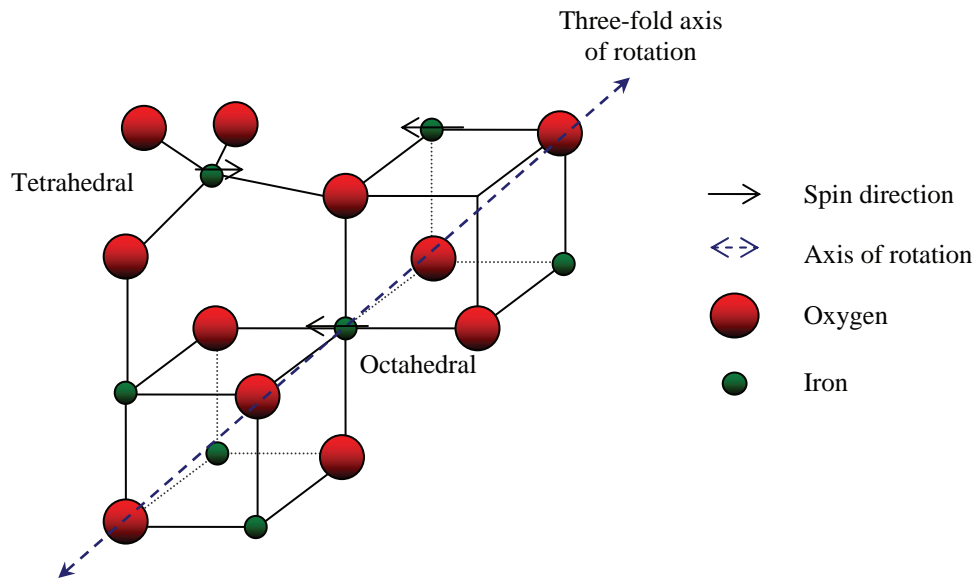

Figure 1. A portion of the inverse spinel structure of Fe_3O_4 , where iron(II) and iron (III) ions are indicated as small (green) dots and the larger oxide anions are indicated as red dots.[42]

Furthermore, as illustrated in *Figure 1*, the electron spins of Fe^{3+} ions in octahedral interstices are aligned antiparallel to those in tetrahedral interstices, and hence no net magnetization is observed from these ions. The Fe^{2+} ions tend to align their spins parallel to those of Fe^{3+} ions in adjacent octahedral sites leading to a net magnetization.

_____

1.2.3 Superparamagnetism associated with Fe_3O_4 nanoparticles

The problem with nano-sized Fe_3O_4 materials is that the individual nanoparticles possess high surface energies, because of their large ratio of surface area to volume.[67] For this reason, they have the tendency to interact with each other forming large aggregates in order to minimize their total surface energy. Moreover, because the Fe_3O_4 nanoparticles are magnetic by nature, there is an additional contribution from strong, short range inter-particle magnetic dipole-dipole forces that further facilitates aggregate formation as illustrated in *Figure 3*.
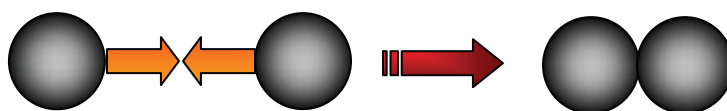

Figure 3. Illustration of aggregate formation caused by inter-particle magnetic coupling forces.

However, when the diameter of the Fe_3O_4 nanoparticles is reduced to below a certain critical value (usually less than 35 nm), they lose their bulk ferromagnetism and are said to become superparamagnetic.[68,69] Superparamagnetism is associated with finite size and surface effects that dominate the magnetic behavior of individual nanoparticles.[42,64] This phenomenon of superparamagnetism arises when the thermal energy within magnetic domains is sufficient to overcome the magnetic coupling forces between the nanoparticles, causing their atomic magnetic dipoles to fluctuate randomly. When an external magnetic field is applied, the nanoparticles acquire a certain magnetization, but because of the high thermal energy, the long range order is lost when the field is removed and the nanoparticles have no remanent magnetization.[64-66]
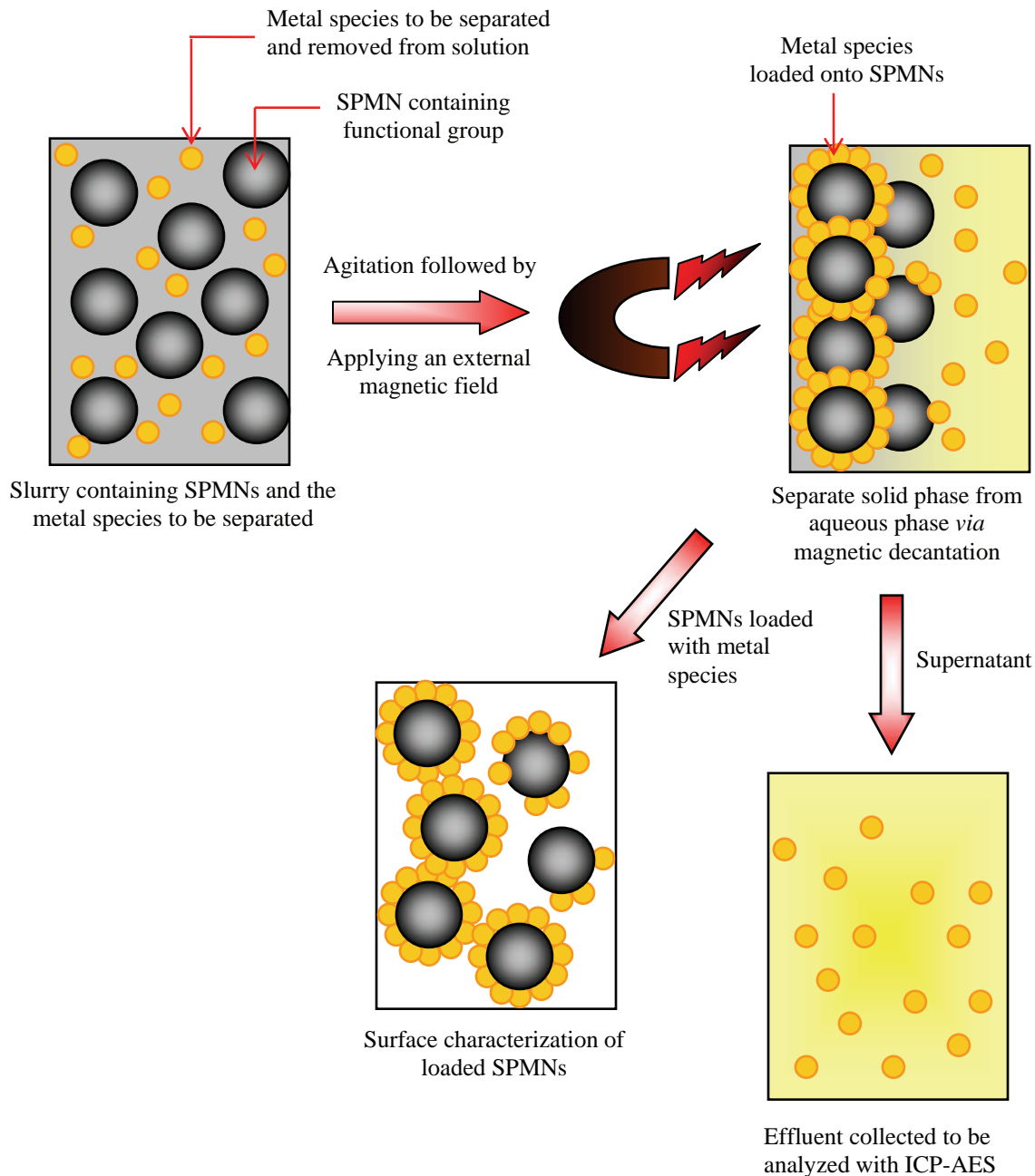
The superparamagnetic properties of Fe_3O_4 nanoparticles are unusual because they represent single magnetic domains as illustrated in *Figure 4*. The ordering of electron spins characteristic of magnetic nanoparticles leads to the formation of regions of magnetic alignment called the domains.[42,64] Thus a magnetic domain describes a region within a material which has uniform magnetization. The nanoparticles can become magnetized when the magnetic domains within the material are magnetized and aligned. This can be done by applying a moderate external magnetic field or by passing an electrical current through the bulk material, so that individual magnetic domains tend to align in the same direction as the external field. Some or all of the domains can be aligned. The more domains that are aligned the stronger the resultant magnetization of the material. When all of the domains are aligned, the material is said to be magnetically saturated.

_____

It is important to point out that zero coercivity and zero remanance (*i.e.* no hysteresis effect) on the magnetization curve indicate that the material is superparamagnetic in nature as indicated by the dotted lines in *Figure 5*. Shown in *Scheme 3* is an illustration of the superparamagnetic behavior (characteristic "spiking") of organic-based ferrofluid suspended in an aqueous phase. The ferrofluid was obtained by coating and thus sterically stabilizing synthesized SPMNs with surfactant molecules (oleic acid). Kerosene was used as an organic medium. The external magnetic field source used to manipulate the superparamagnetic ferrofluid is a small ferrite magnet.
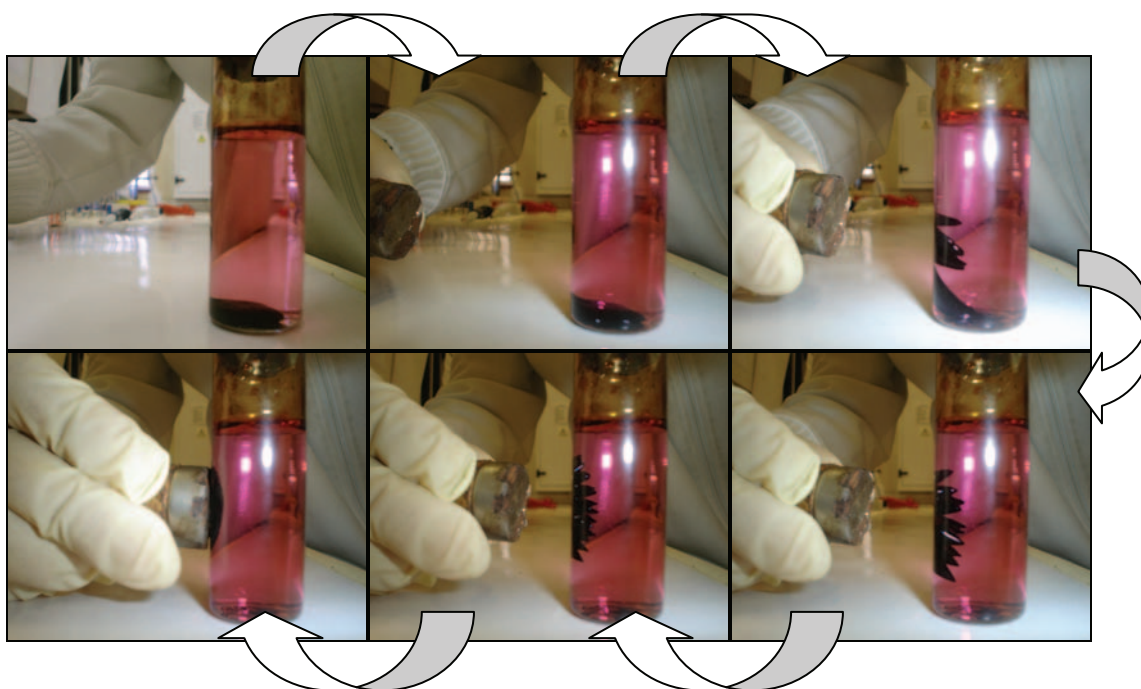
Scheme 3. Superparamagnetism of a Fe_3O_4 based ferrofluid suspended in an aqueous phase.

With the advancements of material science especially in the area of nano-materials, efforts have been made to alter the nanoparticle properties for specific applications. Recently, various approaches have been reported for the fabrication of SPMNs. Since SPMNs, silica coated SPMNs and also modified silica coated SPMNs were synthesized for our application, it is essential to give the reader background information regarding these synthetic procedures.

_____

Metal species to be separated
and removed from solution

SPMN containing
functional group

Metal species
loaded onto SPMNs

Agitation followed by

Applying an external
magnetic field

Slurry containing SPMNs and the
metal species to be separated

Separate solid phase from
aqueous phase *via*
magnetic decantation

SPMNs loaded
with metal
species

Supernatant

Surface characterization of
loaded SPMNs

Effluent collected to be
analyzed with ICP-AES

*Scheme 4. Illustration of magnetic separation of solid phase containing the adsorbed metal
species from the aqueous phase.*

_____

solution. 0.4 mL tetraethyl orthosilicate (TEOS) was added to this mixture and stirred with a mechanical agitator. After 24 h, a further 0.7 mL was added to the suspension and stirred for a further 2h. The silica-coated particles obtained were then washed with an 80 % ethanol-water (v/v) solution and the excess liquid removed while retaining the SPMNs *via* magnetic decantation. The silica-coated SPMNs were dried by evaporation of the solvent at room temperature.

For simplicity, the silica-coated SPMNs will be referred to as FeSi nanoparticles. A simplified representation of the formation of silica-coated SPMNs is illustrated in *Scheme 5*.

One Fe₃O₄ nanoparticle   *Silica precursor molecule, TEOS*   *Formation of FeSi nanoparticle*
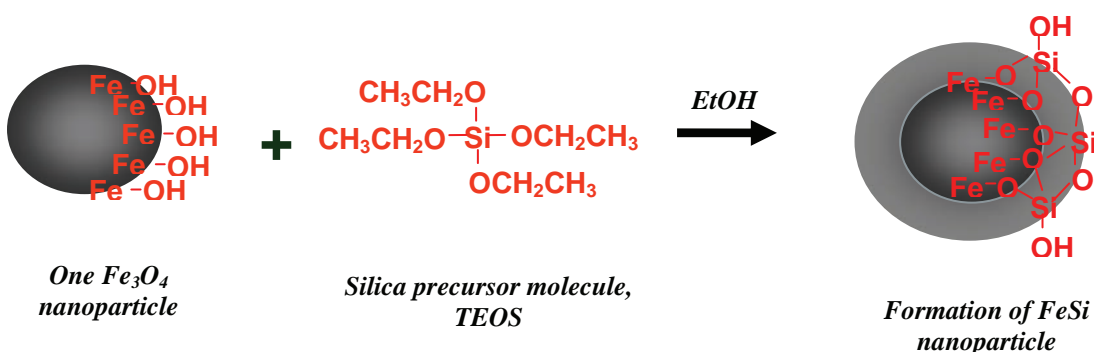
Scheme 5. Illustration of silica coating procedure onto surface of SPMN.

In the sol-gel process reported above, the hydrolysis of the silica precursor (TEOS) in the presence of a base produces silanol (Si-OH) entities, which on further condensation produces a sol.[84,89] Hydrolysis and condensation are simultaneous processes. In these basic conditions, condensation is accelerated relative to hydrolysis reactions and siloxane linkages (Si-O-Si) are formed. Thus, a highly branched silica network with ring structure was formed. For the purpose of our work, SPMNs were coated with silica to prevent them from agglomeration but also to avoid possible slow dissolution when SPMNs are exposed to acidic solutions.

2.2.3 Surface functionalization of silica-coated SPMNs with trimethoxysilyl alkylamines

The silica surface of silica-coated SPMNs (FeSi) was functionalized with amine trimethoxysilane ligands *via* a methanolysis reaction (*Scheme 6*).[12,28,38] The ligand immobilization procedure was typically as follows: 60 mg of FeSi particles were re-suspended in 600 µL ethanol (5 – 10 mL solvent/g FeSi) followed by addition of the suspension 1.7 mmol free amine ligand per gram FeSi particles. The amine trimethoxysilane ligands used in this study for surface functionalization were

_____

3-(trimethoxysilyl) propylamine (APTS) to yield monoamine silica-coated SPMN nanocomposite material; N-[3-(trimethoxysilyl) propyl] ethylenediamine (ED) to yield diamine silica-coated SPMN nanocomposite material, respectively. After stirring for 48 h, the residual reagents were removed by washing the mixture with an 80 % ethanol-water (v/v) solution *via* magnetic decantation and the material dried by evaporation of the solvent at ambient temperature.

The amine-functionalized silica-coated SPMN nanocomposite materials will be referred to as **(1)** FeSiAPTS and **(2)** FeSiED, to denote the monoamine functionalized and the diamine functionalized silica-coated SPMNs, respectively. The summary of the surface functionalization to yield **(1)** FeSiAPTS and **(2)** FeSiED nanocomposite materials is shown in *Scheme 6* below.
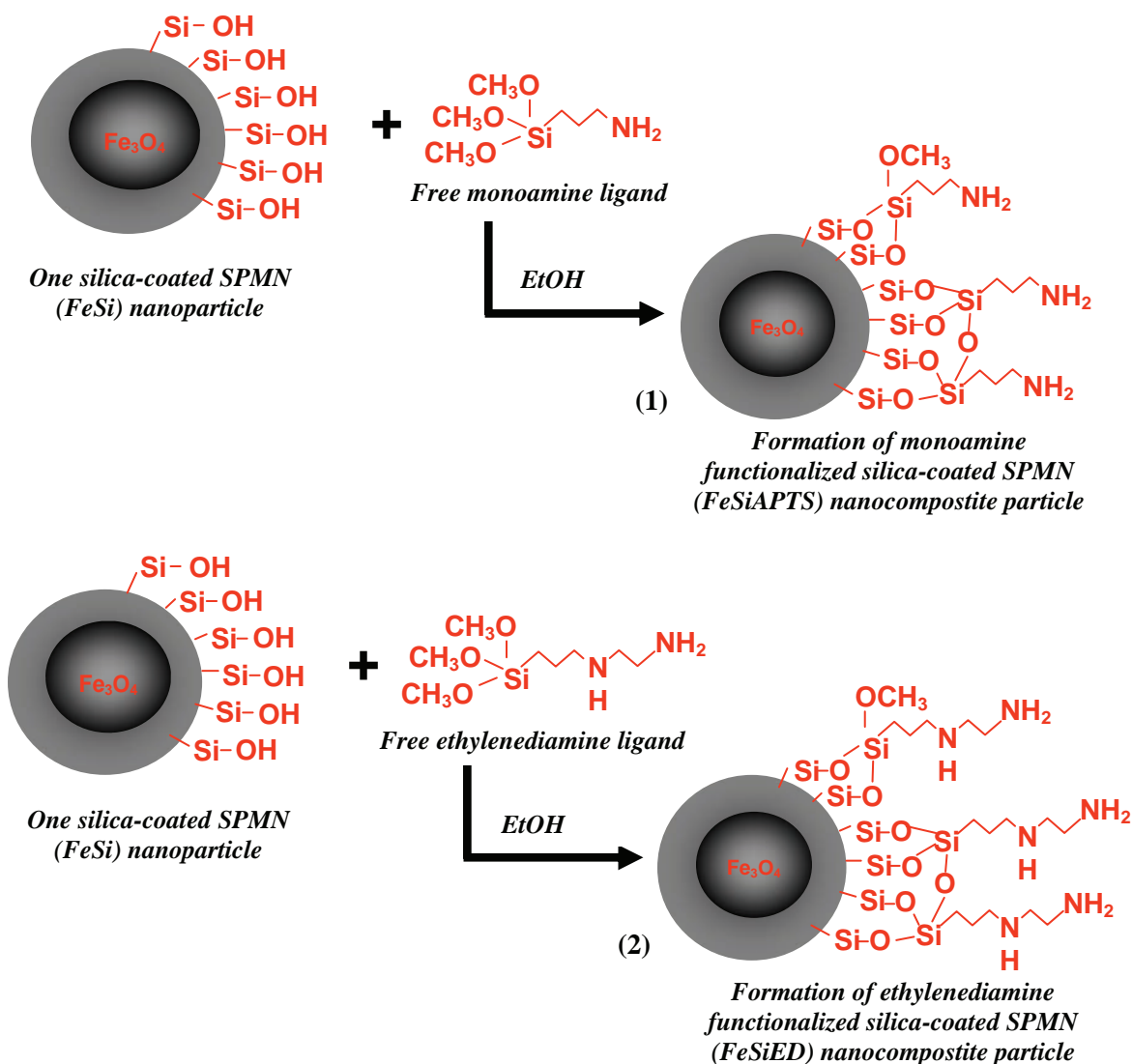
Scheme 6. Immobilization of free amine-containing ligands onto silica-coated SPMNs.

Although it is clear that the bulk of the particles consist mainly of Fe_3O_4 phase, there is some evidence of other impurities in the samples, labeled as '*' in the XRD pattern in *Figure 6*. The impurities can be attributed to the hematite (α-Fe_2O_3) phase.

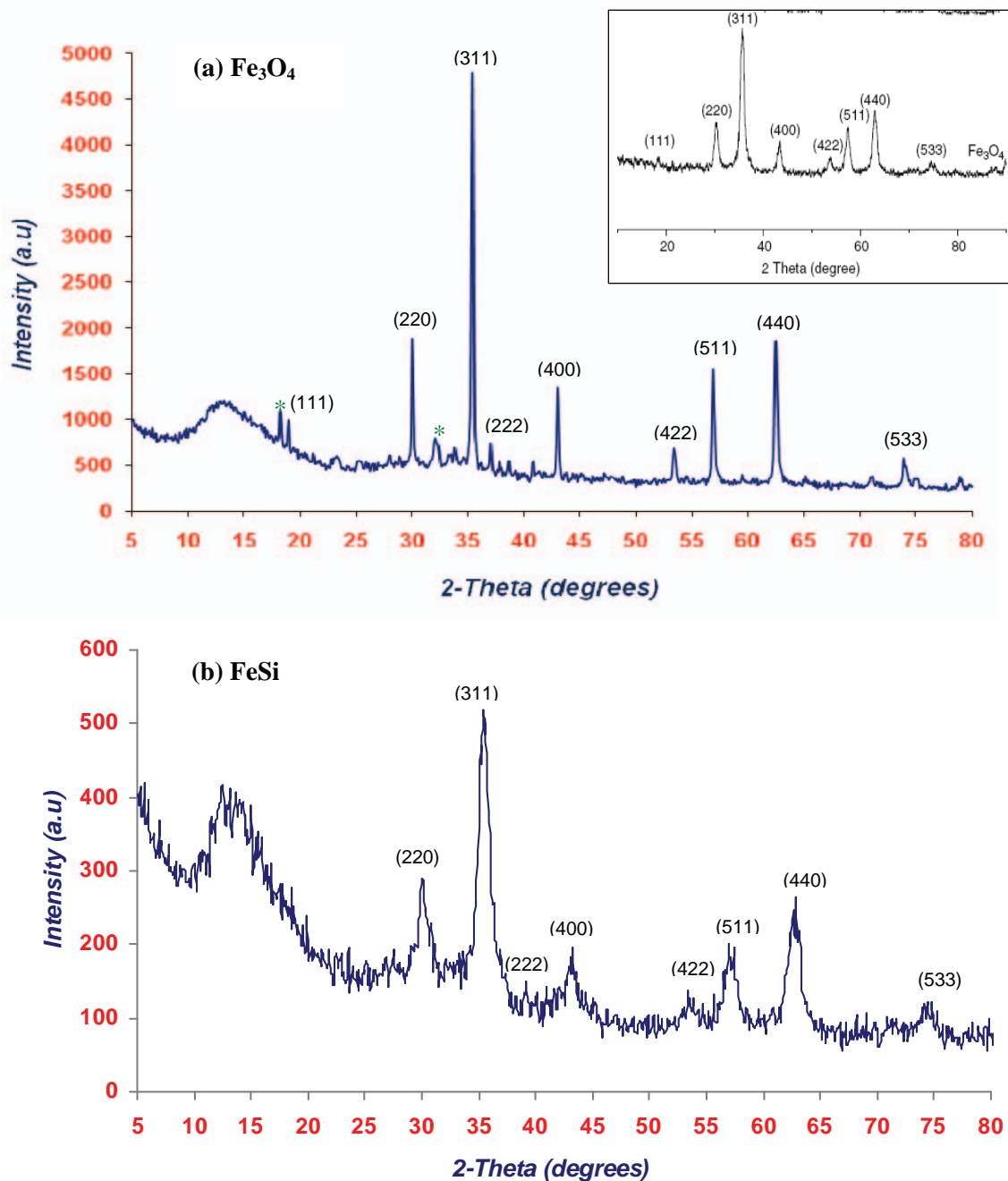*Figure 6. Indexed X-ray diffractograms of (a) uncoated Fe_3O_4 and (b) FeSi nanomaterials with different particle sizes. '*' indicates lines from α-Fe_2O_3 impurity phase(s). The relative intensity of the patterns is related to the degree of crystallinity of the materials. The obtained spectra were corrected for instrumental line broadening and refined with the XRD analysis program EVA.[128] Shown in the inset is a reference XRD pattern.[116]*

the above mentioned factors. These images were collected 48 h after the suspension preparation, which could have resulted in the loss of SPMN suspension stability with time, thus causing the observed agglomeration.[1] Evidence of colloid instability was the sediment which formed in the vials consisting of the colloidal aqueous SPMN suspensions which were analyzed after 48 h.

The mean diameter and size distribution was determined by measuring more than 150 individual SPMNs from the TEM micrographs obtained using *Image J*, a public domain image processing program.[109] The corresponding histograms of the respective size-distributions of each TEM micrograph is shown in *Figure 8 (a) and (b)*. Monodispersed SPMNs with an average particle diameter of 9.04 ± 1.23 nm for route B and 5.20 ± 0.66 nm for route A, respectively were obtained. The experimental results thus show that flowing nitrogen gas through the aqueous reaction medium as was done in route A, not only protects against critical oxidation of the SPMNs but also reduces the particle size when compared with route B, without removing the dissolved oxygen in the reaction medium. As was found in this study the SPMN size was reduced from approximately 9 nm (route B - aerobic conditions) to 5 nm (route A - anaerobic conditions) as shown by the size distribution histograms in *Figure 8 (a) and (b)*.
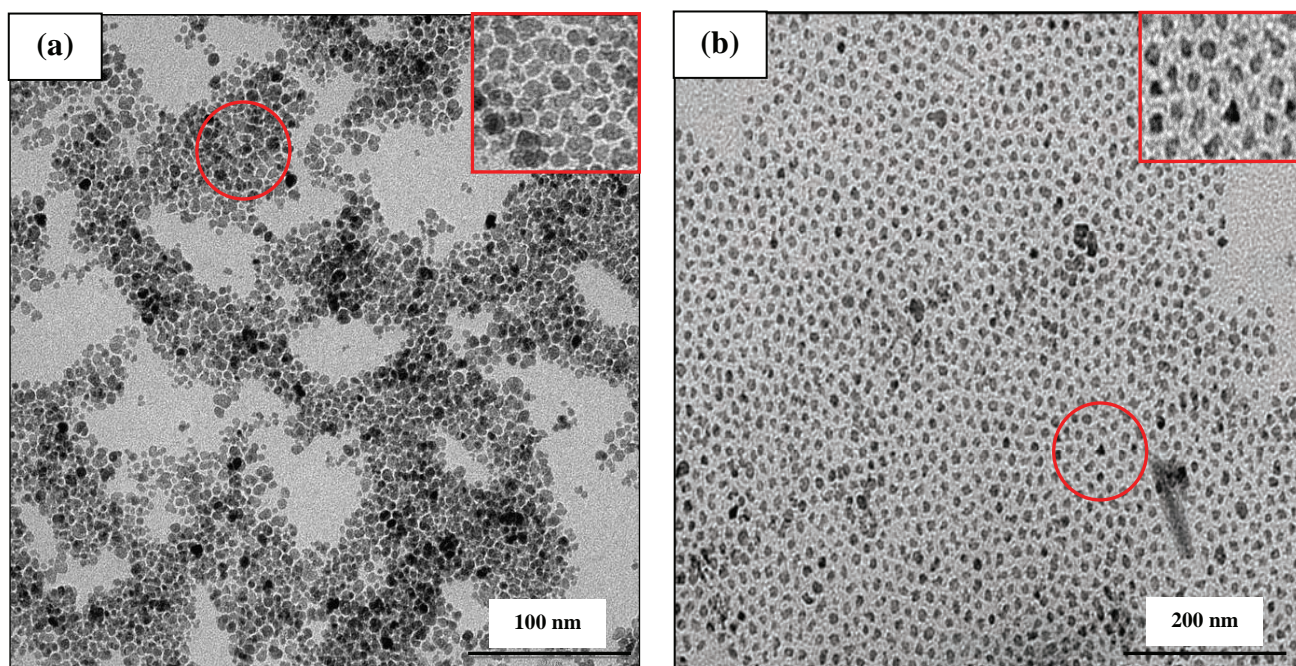
Figure 7. TEM micrographs of SPMNs prepared under (a) aerobic and (b) anaerobic conditions. The inset shown in each micrograph is a magnification illustrating the morphology of the SPMNs.

---

[1] These TEM analyses were not done at Stellenbosch University, so this delay was unavoidable.
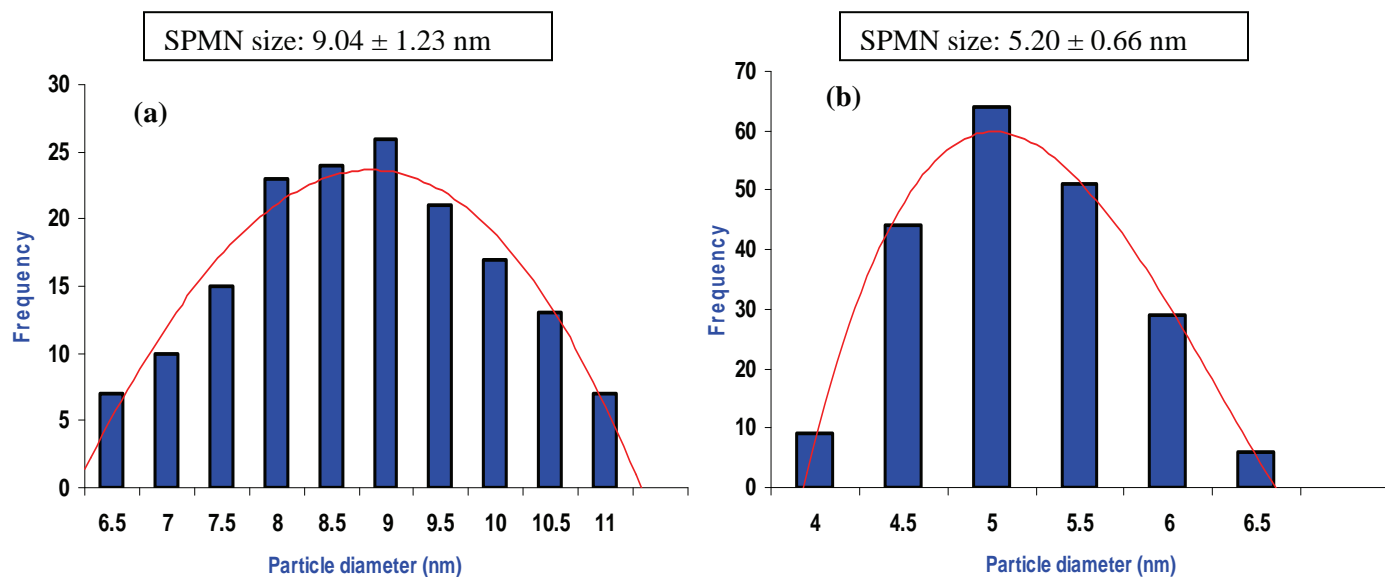
_____

Figure 8. Size distribution histograms of SPMNs synthesized under (a) aerobic and (b) anaerobic conditions. The histograms correspond to the TEM micrographs shown in Fig. 7.

3.1.2.2 Morphology and size of silica-coated SPMNs

The silica coating around the SPMNs was also examined using TEM. The SPMNs used as seeds in the silica coating procedures were those obtained from the synthetic route B. The TEM micrographs of the silica-coated SPMNs (FeSi nanoparticles) prepared using different volumes of TEOS precursor are shown in *Figure 9 (a – c)*. The TEM micrographs (*Figure 9 (a – c)*) were obtained using 0.4 mL, 0.6 mL, and 0.8 mL TEOS precursor, respectively as described in *Chapter 2, section 2.2.2*. According to the micrographs, the morphology of the obtained FeSi nanoparticles varied from spherical to irregular with clear evidence of SPMN aggregation and silica cluster formation as indicated by the red arrows in the micrographs. In *Figure 9 (a) and (b)*, two regions with different electron densities can be distinguished for the FeSi nanoparticles: an electron dense region which presumably corresponds to SPMN core(s), and a less dense, more translucent region surrounding these cores, that is likely to be the silica coating shell. This might be described as SPMN-silica core-shell structures. Thus, *Figure 9 (a)* and (b) illustrates that a silica layer was formed around the small aggregates of several SPMNs. The formation of small aggregates of SPMNs resulted from the magnetic dipolar interaction among the individual SPMNs. Coating such aggregates with a silica layer could reduce the magnetic dipolar interaction and further promote the stability of SPMNs.[96]
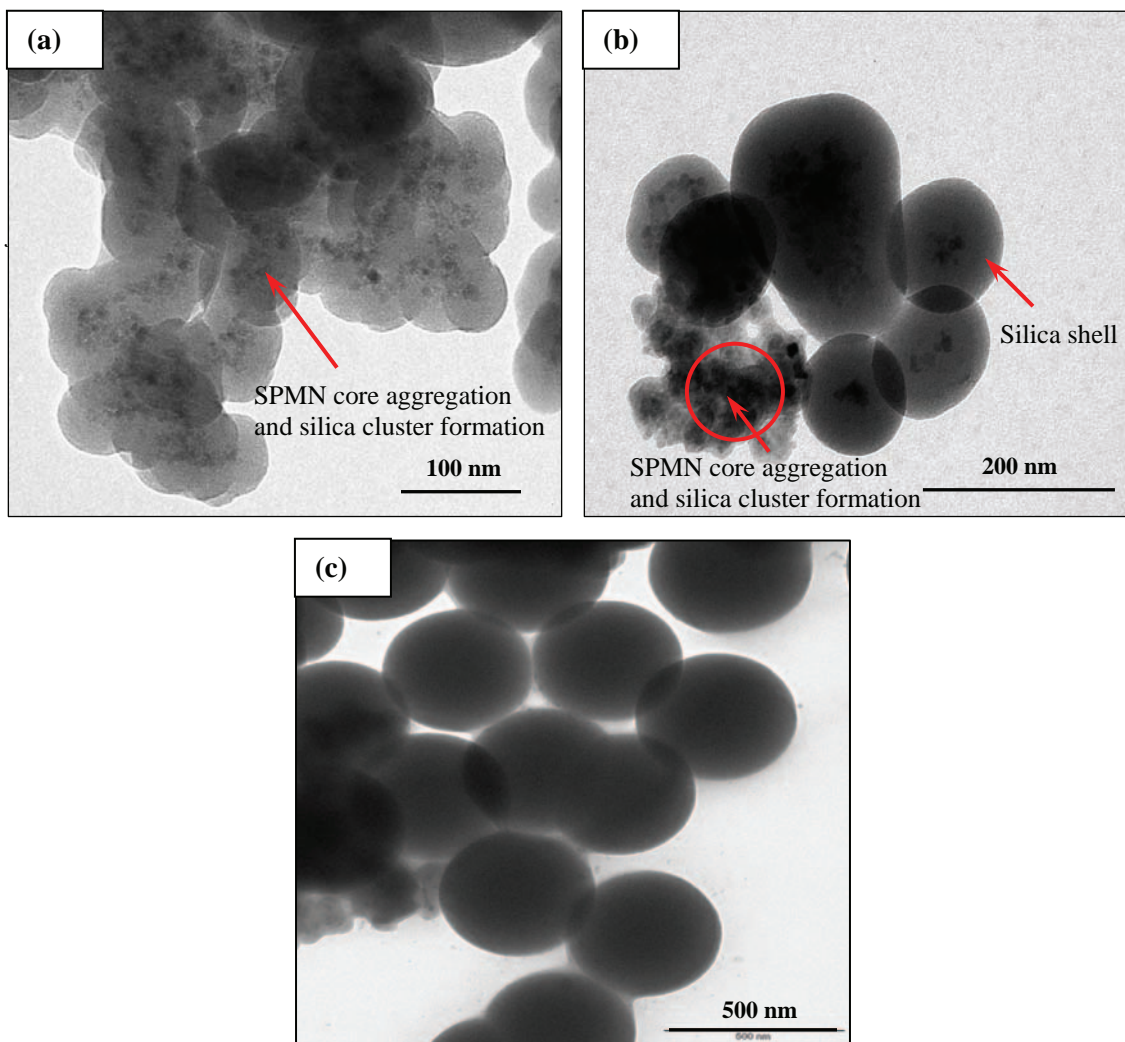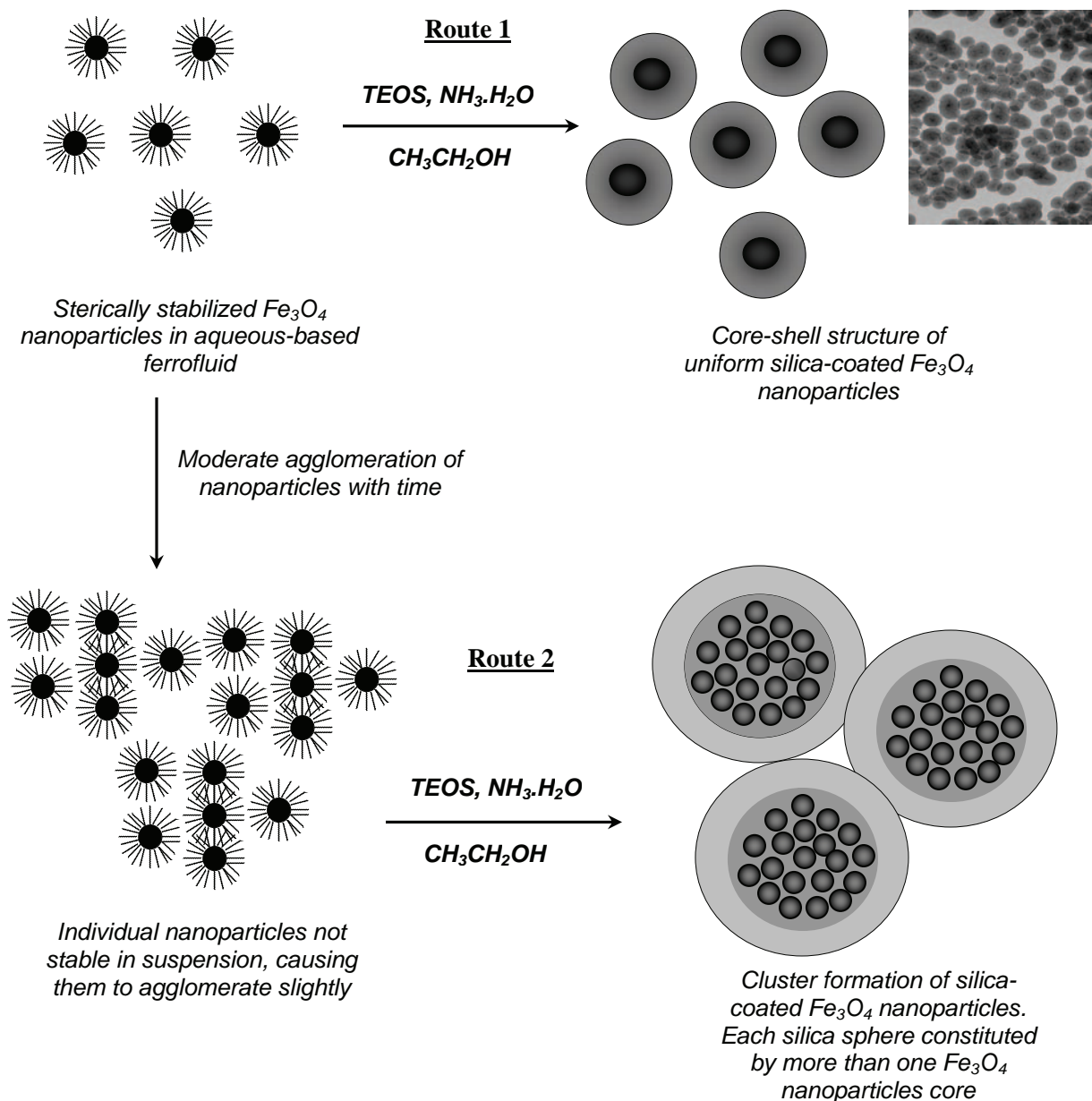
_____

Figure 9. TEM micrographs of silica-coated SPMNs illustrating morphology, size, aggregation and cluster formation. Different volumes of TEOS precursor added: (a) 0.4 mL, (b) 0.6 mL, and (c) 0.8 mL.

It was very difficult to evaluate the thickness of the silica coated shell because of silica cluster formation and due to the poor contrast between this amorphous protective shell and the cores of the SPMNs. Therefore, it was not possible to construct a reliable size distribution histogram of the formed FeSi nanoparticles. However, *Figure 9 (a) and (b)* suggested that the silica coated shell was fairly homogeneous and the thickness was estimated to be in the range 80 – 120 nm.

As can be seen from *Figure 9 (a – c)*, there is a distinct difference in the size of the FeSi nanoparticles obtained. It was found that with increased volumes of the TEOS precursor used during the silica coating procedure from 0.4 mL to 0.8 mL, the thickness of the silica shell increased.

_____

Scheme 8 is the two possible routes as mentioned above during silica coating formation. Route 1 illustrates the formation of nicely separated monodispersed FeSi nanocomposite materials with core-shell structure. Route 2 illustrates more or less what happened in our silica coating process, ill-defined and agglomerated SPMN-silica nanocomposite materials.

Route 1

TEOS, NH$_3$.H$_2$O

CH$_3$CH$_2$OH

Sterically stabilized Fe$_3$O$_4$ nanoparticles in aqueous-based ferrofluid

Core-shell structure of uniform silica-coated Fe$_3$O$_4$ nanoparticles

Moderate agglomeration of nanoparticles with time

Route 2

TEOS, NH$_3$.H$_2$O

CH$_3$CH$_2$OH

Individual nanoparticles not stable in suspension, causing them to agglomerate slightly

Cluster formation of silica-coated Fe$_3$O$_4$ nanoparticles. Each silica sphere constituted by more than one Fe$_3$O$_4$ nanoparticles core

Scheme 8. Simplified representation of the silica-coating of the SPMNs illustrating the ideal (top route)[27] and non-ideal (bottom route) situation during the coating procedure.

_____

3.1.3 Elemental composition analysis

3.1.3.1 Energy dispersive X-ray spectroscopy

To confirm the presence of the main elements in the synthesized materials, an elemental composition analysis was done by energy dispersive X-ray spectroscopy (EDX). Using this technique, the elemental composition of the materials was obtained with high resolution. EDX analysis data confirms that the main components of the materials **(1)** and **(2)** are Fe, Si, O, N and C (*Figure 10*). The presence of silica in the samples confirmed the protective amorphous silica coating for the SPMNs and the presence of C and N in particular confirmed the functionalization of the silica-coated SPMN nanocomposite materials with the amine ligands.
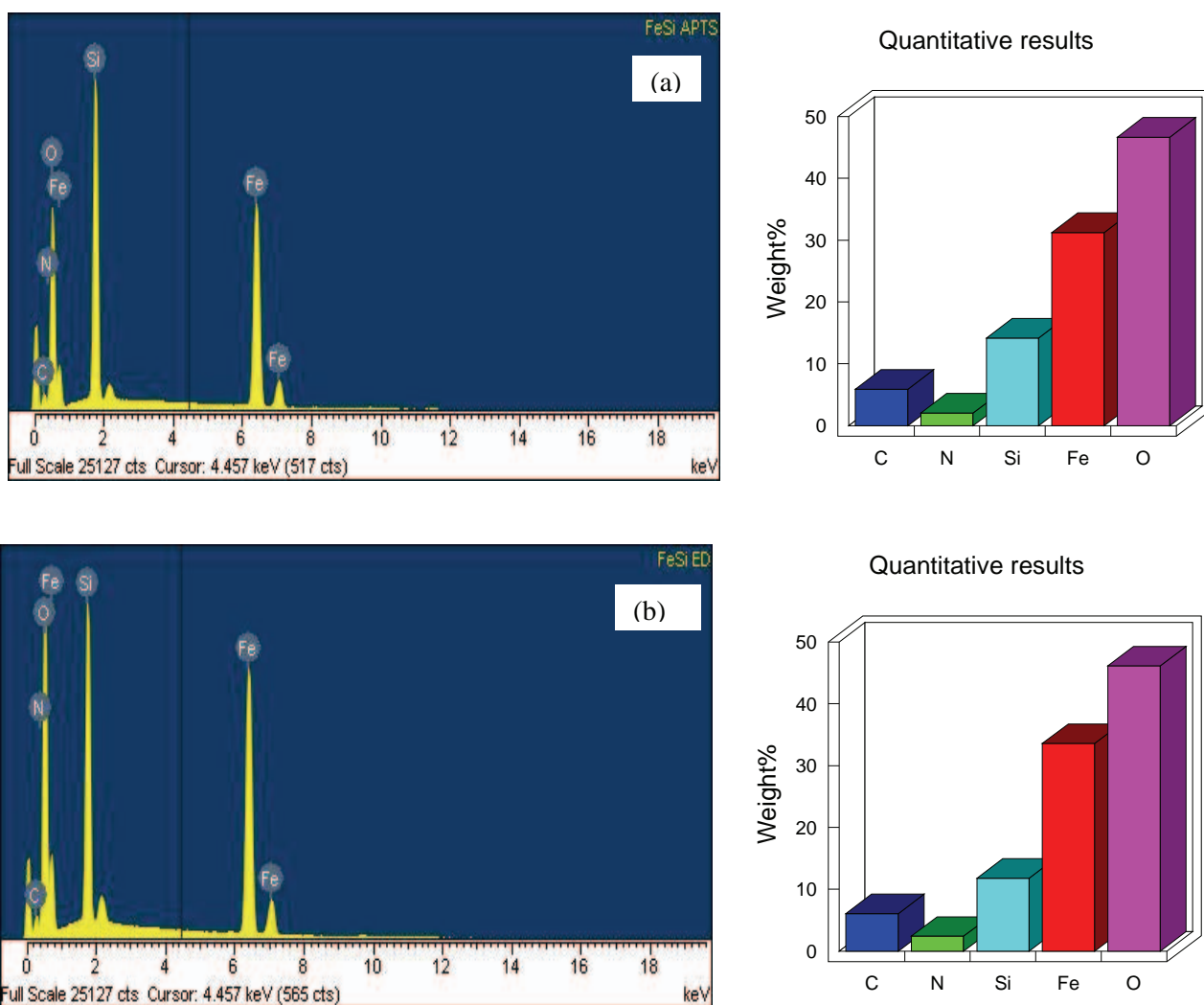
*Figure 10. EDX analysis images of the amine-functionalized silica coated SPMN materials.
(a) material (**1**) FeSiAPTS, and (b) material (**2**) FeSiED.*

_____

3.1.3.2 Elemental (C, H, and N) analysis

Surface modification of SPMNs and silica surfaces with organosilanes has been extensively studied as discussed in *Chapter 1, section 1.2.5.3*. Through hydrolysis of the alkoxy group (usually methoxy or ethoxy), the silane molecules are attached to the particles surfaces *via* covalent bonding and terminated with functional groups such as amines. In this work, silica-coated SPMNs (FeSi) were functionalized with amine trimethoxysilane ligands to produce magnetic ion-exchanger nanocomposite materials with (**1**) monoamine and (**2**) diamine functionality.[12,28,38] These materials are presented below in *Figure 11*. For simplicity, these amine functionalized silica-coated SPMNs are referred to as (**1**) FeSiAPTS and (**2**) FeSiED. (*Refer to Chapter 2, section 2.2.3 for experimental procedures*).

Elemental analysis (C, H, and N) was done on these materials in order to determine the amount of amine ligand that was immobilized onto the surface of silica-coated SPMNs (FeSi). The ligand concentrations of materials (**1**) and (**2**) were calculated from the weight percentage of nitrogen, as is generally done while carbon and hydrogen percentages, which are based on this ligand concentration, are given in parentheses (*Tables 2 and 3*). (Refer to *supplementary section A1* for the calculations of the obtained values). In each table are shown results that were obtained from three sets of analysis of different batches of the same material synthesized under similar experimental conditions. As was observed previously, the ligands are grafted on average, *via* two methoxy groups.[12,28,101] This was confirmed by our results.
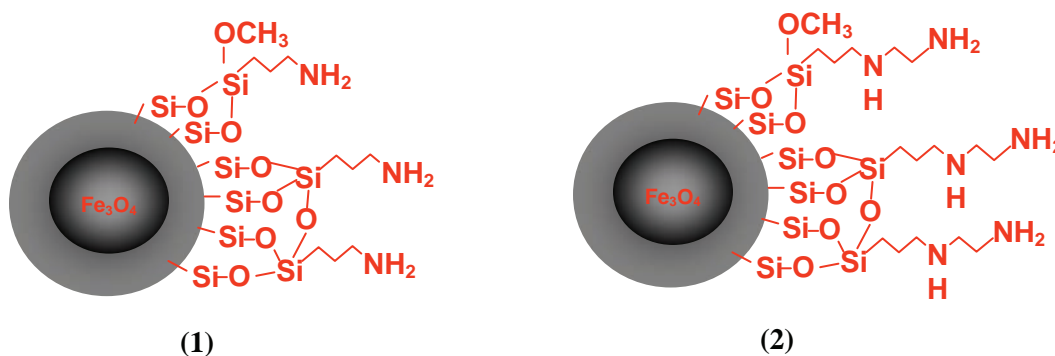
*Figure 11. Illustration of the monoamine (**1**) FeSiAPTS, and ethylenediamine (**2**) FeSiED functionalized FeSi nanocomposite materials.*

_____

were some discrepancies between the experimental and calculated values of the H percentage in each sample. These differences could be attributed to residual water in the samples.

From these results it could be concluded that the FeSi materials were successfully functionalized with the amine ligands and that the immobilization onto the surface occurred *via* two methoxy groups. However, the ligands could also be immobilized onto the FeSi surface *via* *all* three methoxy groups, depending on the experimental conditions used in this process.

3.1.4 Surface characterization
3.1.4.1 Thermogravimetric analysis

The percent weight loss as a function of temperature was studied by TGA for unfunctionalized SPMNs and for the functionalized silica-coated SPMN materials. The purpose of these studies was to investigate the decomposition of the materials, to gain some structural knowledge, and also to comparatively determine the amount of amine ligands grafted onto the surface of the silica-coated SPMNs. As can be observed from *Figure 12*, the TGA curve of the unfunctionalized SPMNs shows a weight loss over the range 90 – 280 ºC of about 3 %. This loss can be attributed to the loss of adsorbed water and dehydroxylation of internal OH⁻ groups according the *Scheme 9*.
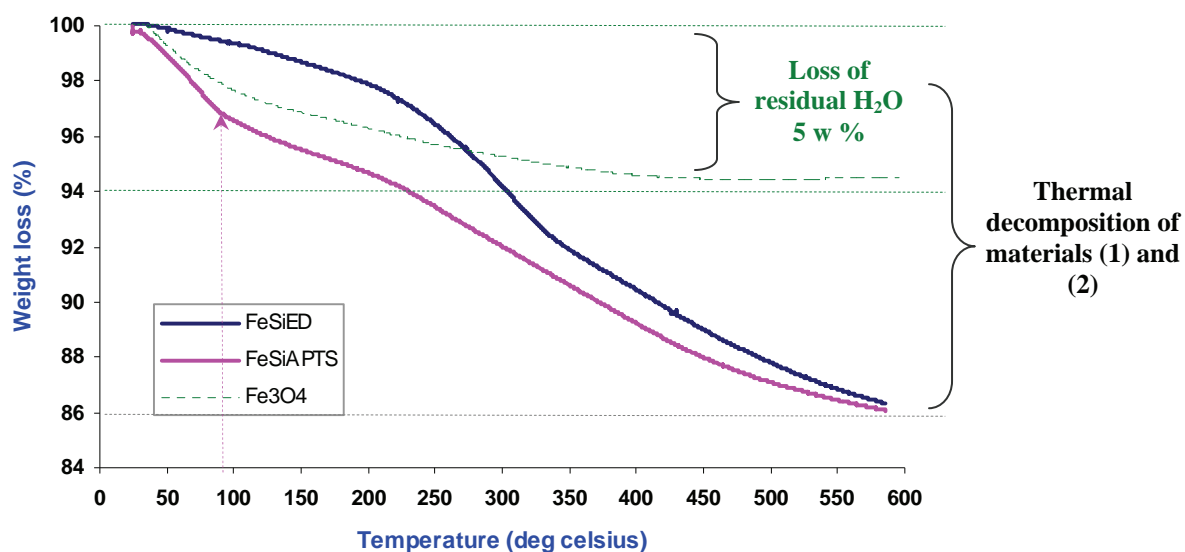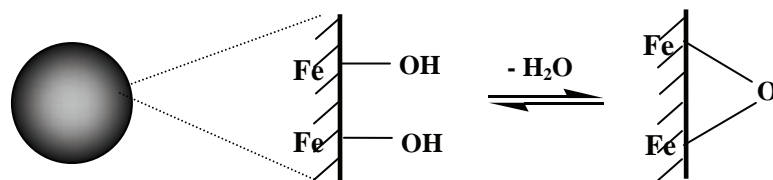

*Figure 12. TGA curves of SPMNs, and of materials (**1**) FeSiAPTS and (**2**) FeSiED.*

_____

Scheme 9. Illustration of the loss of absorbed H₂O from the SPMN surface.

The TGA curves of **(1)** FeSiAPTS and **(2)** FeSiED show two weight loss steps. The first weight loss for **(1)** is over the range 100 – 225 ℃ which can be due to the loss of residual water (dehydration process) adsorbed physically in the material. For **(2)** there is a weight loss over the range 125 – 250 ℃ which is due to material decomposition, since there is no evidence of residual water losses (*Figure 12*). The second weight loss step for **(1)** is over the range 225 – 590 ℃ and for **(2)** over the range 250 – 590 ℃. These losses can be ascribed to even further decomposition of the materials. The total weight losses are approximately 10 % and 14 % for **(1)** and **(2)**, respectively.

If assumed that the total weight loss is only due to the amount of amine ligands on the surface of **(1)** and **(2)**, then from the data obtained, the relative amount of monoamine and diamine methoxy silane ligands immobilized onto the surface of the silica-coated SPMN materials was calculated and found to be 0.56 and 0.63 mmol/g for **(1)** and **(2)**, respectively. From the TGA data obtained, we could estimate that the surface of **(1)** was approximately 27.45 % functionalized and that the surface of **(2)** was approximately 30.91 % functionalized with the ligands.

The average ligand concentration obtained from elemental analysis calculations was found to be 0.75 mmol/g and 0.87 mmol/g for **(1)** and **(2)**, respectively (see *3.1.3.2*). These discrepancies between the ligand concentration values obtained from the different analysis methods could be due to the differences in pore sizes of the silica-coated SPMNs, ligands fit differently through the pores. As a result, the accessibility of amine groups decreases and accordingly, the ligand concentration. However, it should be pointed out that the results obtained from elemental analysis are much more reliable and therefore these values were accepted as the relative ligand concentrations on the surface of silica-coated SPMNs.

_____

3.1.4.2 Fourier-transform infrared spectroscopy

Fourier transform infrared (FTIR) spectra were acquired to confirm the silica-coating of SPMNs and the subsequent functionalization of these materials with monoamine and diamine methoxysilane ligands. *Figure 13* shows the FT-IR spectra of (a) unfunctionalized SPMNs, (b) monoamine (FeSiAPTS), and (c) diamine (FeSiED) functionalized silica-coated SPMNs. The presence of SPMNs is indicated by the presence of the absorption bands at around 636 cm^{-1} and 474 cm^{-1}. It is known that the FTIR bands at wavenumbers less than 700 cm^{-1} can be assigned to the vibrations of Fe-O bonds of bulk Fe_3O_4.[42,119] Both the unfunctionalized SPMNs, FeSiAPTS and FeSiED showed the presence of Fe-O stretching vibrations at 474 and 636 cm^{-1}. Thus, these bands indicate and confirm the presence of SPMNs. Furthermore, the FTIR spectra of the SPMNs (*Figure 13 a*) show the presence of an O-H stretching vibration due to physisorbed water and potentially surface hydroxyls near 3420 cm^{-1}, and an O-H deformation vibration near 1640 cm^{-1}, respectively. The silica network is adsorbed on the SPMN surface by Fe-O-Si bonds. This absorption band cannot be seen in the FT-IR spectrum because it appears at around 584 cm^{-1} and therefore overlaps with the Fe-O vibration of SPMNs. The sharp absorption band at 1100 cm^{-1} is assigned to the stretching vibration of the Si-O-Si groups.[120,121] The significant features observed for FeSiAPTS and FeSiED are the appearance of the peaks at 3480 and 1642 cm^{-1}. These could be ascribed to the NH_2 stretching vibration and N-H bending mode of free NH_2 groups, respectively. The presence of the anchored propyl groups of FeSiAPTS and FeSiED was confirmed by weak C-H stretching vibrations that appeared at 2880 and 2955 cm^{-1}.[122]
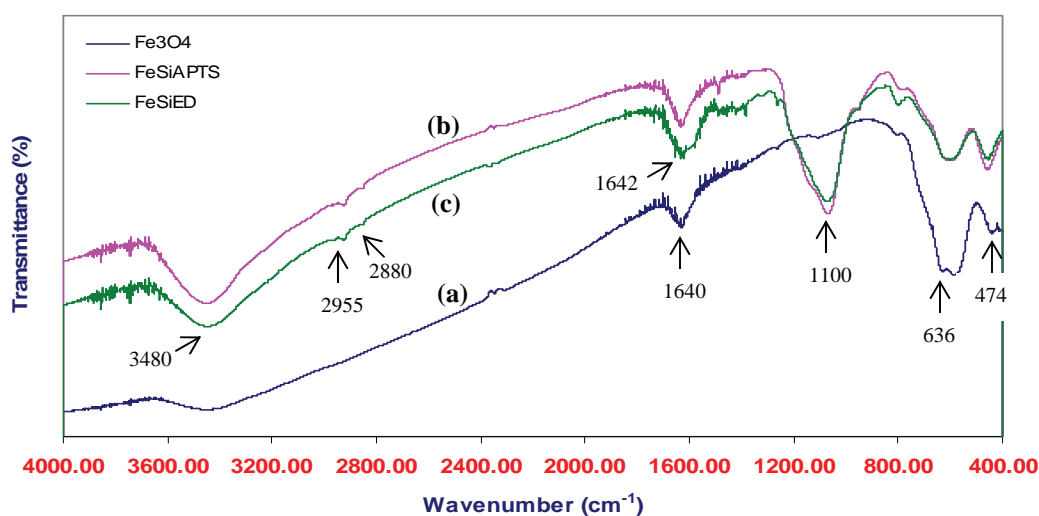
Figure 13. FTIR spectra of (a) unfunctionalized SPMNs, (b) monoamine (FeSiAPTS), and (c) diamine (FeSiED) functionalized silica-coated SPMNs
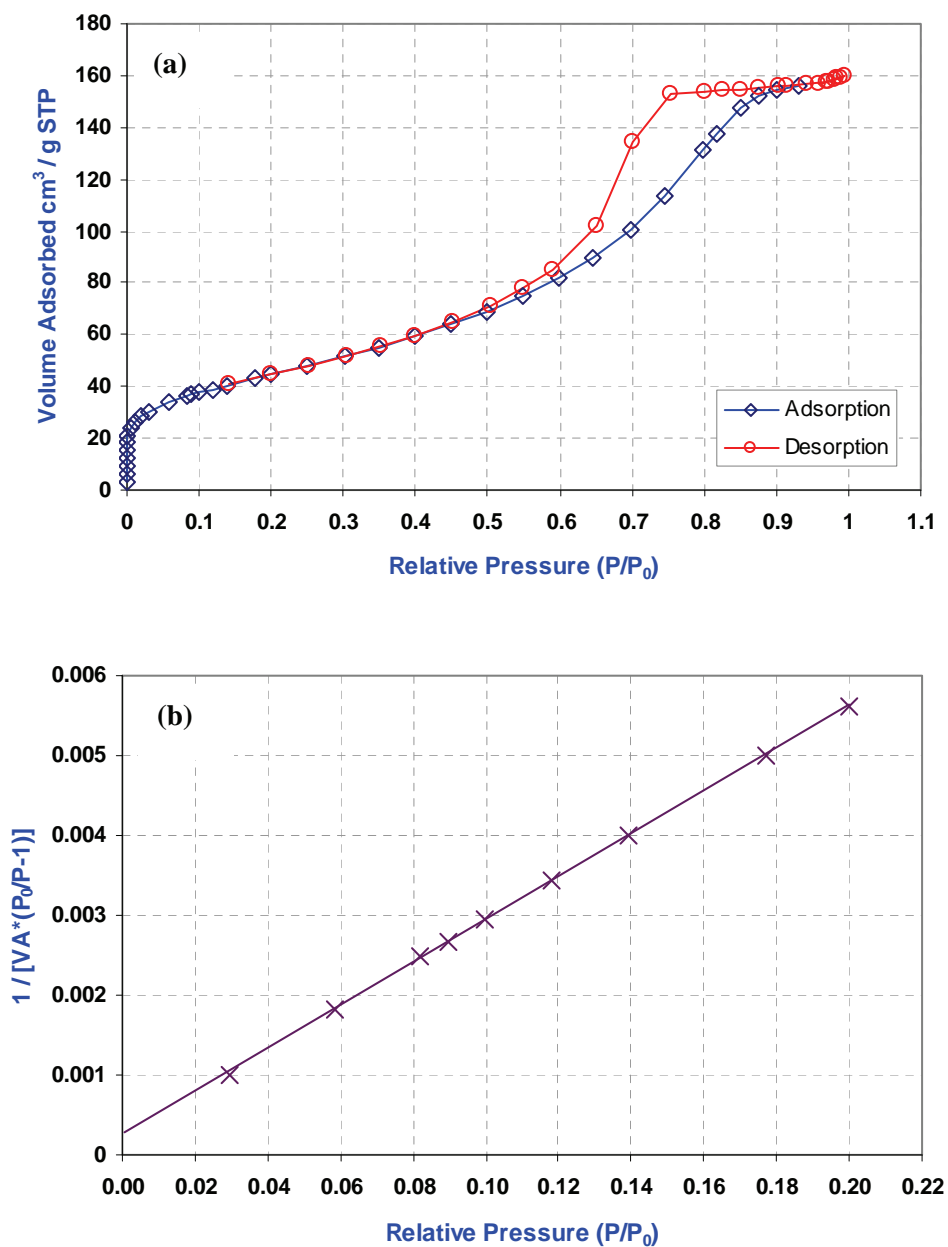
Figure 14. (a) N_2 adsorption- desorption isotherms of SPMN materials, and (b) corresponding BET plot. Surface area: 160 ± 0.77 m^2/g; average pore diameter: 61.12 Å
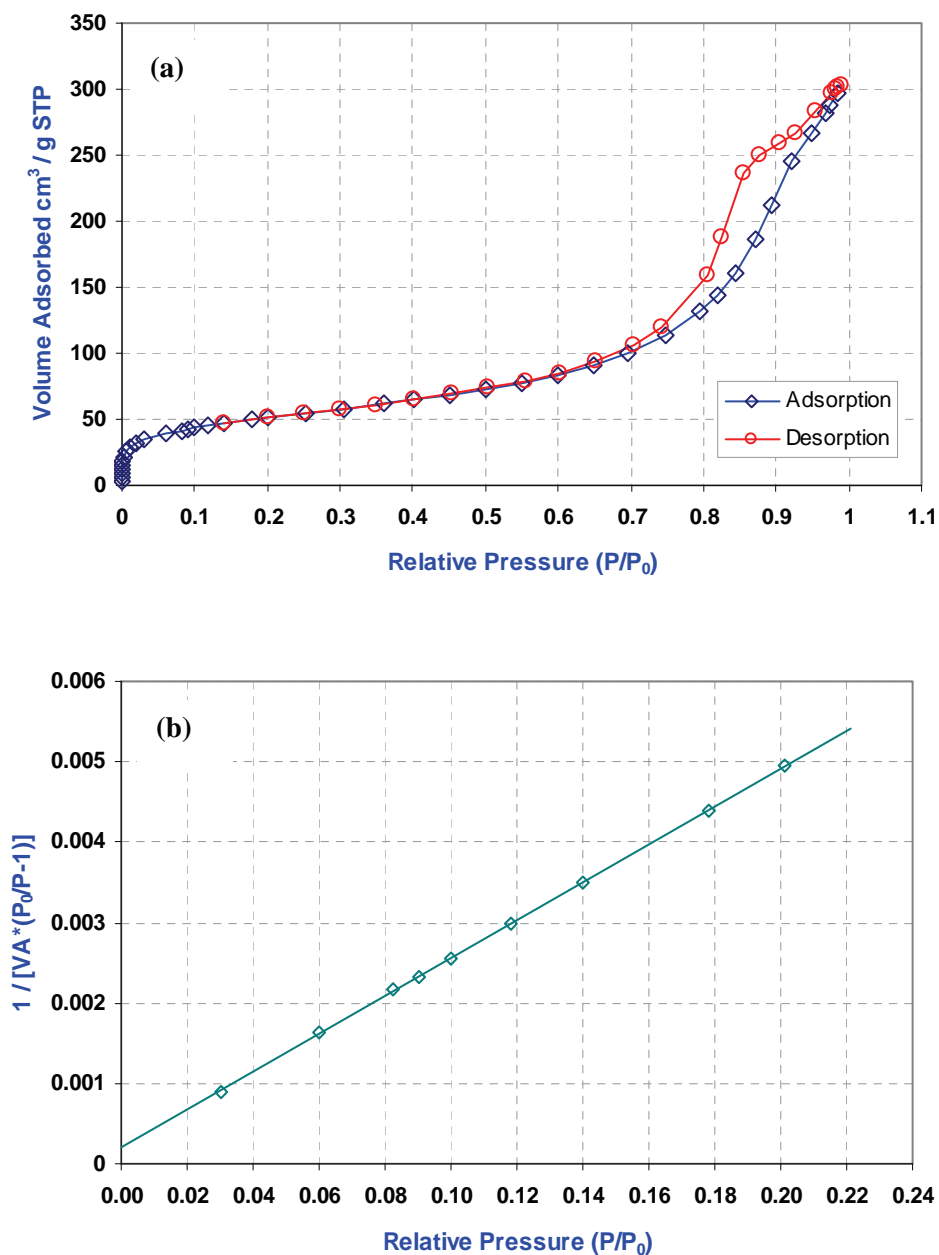
*Figure 15. (a) N_2 adsorption- desorption isotherms of FeSi materials, and
(b) corresponding BET plot. Surface area: 183 ± 0.53 m^2/g; average pore
diameter: 97.16 Å*

As discussed in *Chapter One, section 1.2.4*, zero coercivity and zero remanance (*i.e.* no hysteresis effect) on the magnetization curve shows that the material is superparamagnetic in nature. This was indicated by the dotted lines in *Figure 5*. The magnetization curve the of Fe_3O_4 nanoparticles obtained in this work, is shown in *Figure 16 (a)* and for comparison, a magnetization curve illustrating superparamagnetic behavior of Fe_3O_4 based nanoparticles from literature is shown in *Figure 16 b*.[116]
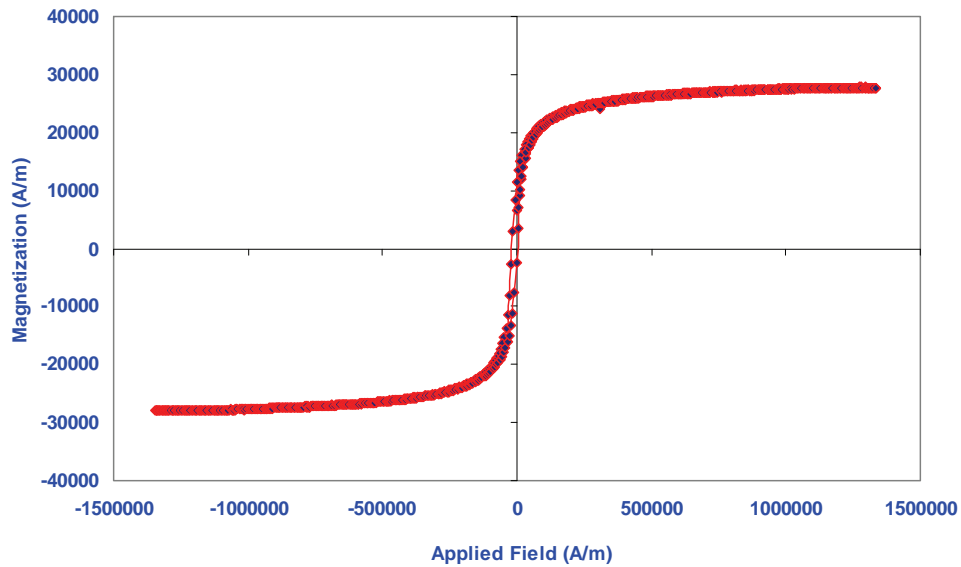
Figure 16 (a). Magnetization curve of Fe_3O_4 nanoparticles illustrating superparamagnetism.
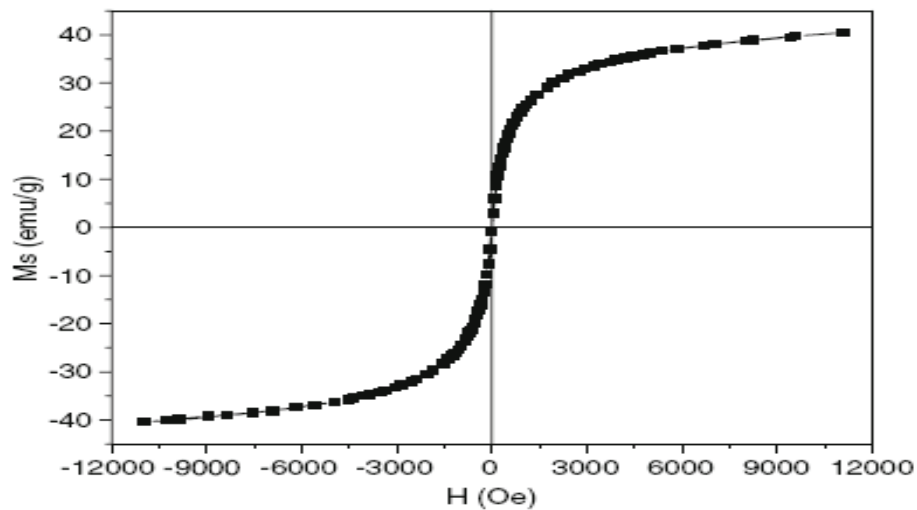
*Figure 16 (b). Magnetization curve from literature of Fe_3O_4 nanoparticles illustrating superparamagnetism.*[116]

4.1 Results and Discussions

4.1.1 Adsorption of complex anions using amine-functionalized silica-coated SPMNs

In this study, we focused on the adsorption of $[PdCl_4]^{2-}$, $[PtCl_4]^{2-}$ and $[AuCl_4]^-$ from dilute HCl solutions using two different amine-functionalized silica-coated SPMN nanocomposite materials, containing (1) monoamine and (2) diamine functionalities. A simplified two-dimensional representation of these magnetic potential anion-exchange materials also referred to as (1) FeSiAPTS and (2) FeSiED is shown below:

(1)   **(2)**
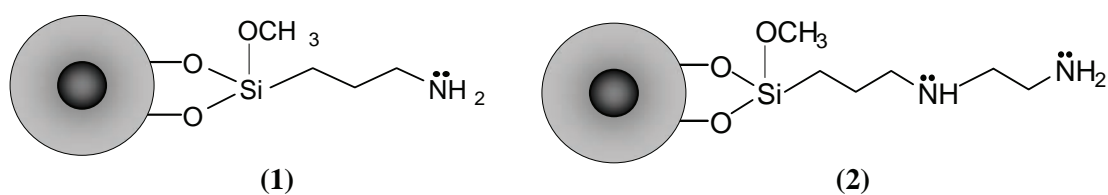
The small black sphere symbolizes the SPMN core, while the pale outer shell represents a layer of silica functionalized by amine methoxysilanes (for simplicity, only one amine ligand grafted onto silica surface is shown). It was found that the amine methoxysilane ligands are grafted on average onto the surface of the silica-coated SPMNs *via* two methoxy groups (*Chapter 3*).

In acidic solutions, the amine moieties of these ion-exchange materials are expected to be protonated. We investigated the possibility that the adsorption of the precious metal anionic complex was due to electrostatic interaction. In this regard, the effect of various experimental conditions and influences on the adsorption capacity was evaluated. All the experiments were carried out by batch sorption experiments at room temperature. Theoretically, in all the cases, the ligand : metal ion molar ratio should allow for complete adsorption of $[PdCl_4]^{2-}$, $[PtCl_4]^{2-}$ and $[AuCl_4]^-$ by materials (1) and (2).

4.1.1.1 Effect of contact time on $[PdCl_4]^{2-}$ and $[PtCl_4]^{2-}$ adsorption

The effect of contact time on the adsorption of $[PdCl_4]^{2-}$ and $[PtCl_4]^{2-}$ was investigated using only the monoamine functionalized material, (1) FeSiAPTS. These experiments were performed to determine the time required to attain equilibrium and to investigate whether (1) had an affinity for these metals under the studied experimental conditions. The time course profiles of sorption for $[PdCl_4]^{2-}$ and $[PtCl_4]^{2-}$ using (1) are shown in *Figure 17*. It should be noted that only 10 mg

_____

samples were used in these batch sorption experiments as given by the experimental conditions in the figure caption. Each adsorption data point (*Figure 17*) was obtained by adding the particular quantity of material to a fixed aliquot of feed solution of known concentration and agitated for a certain amount of time as indicated in the figure. The solid phase was then separated from the aqueous phase and the effluents collected were analyzed for metal ion content *via* ICP-AES. Mass balancing was then used to determine amount of metal adsorbed.

    The results indicate that, as the contact time increased from 3 to 15 minutes, steady state sorption for neither $[PdCl_4]^{2-}$ and $[PtCl_4]^{2-}$ species has been attained. After 30 minutes contact, the quantity of $[PdCl_4]^{2-}$ and $[PtCl_4]^{2-}$ adsorbed remained approximately constant. This indicates that equilibrium between these metal species and the available amine surface sites on **(1)** has been reached and that under the experimental conditions, **(1)** has a low affinity for these PGMs. As can be seen from *Figure 17*, a maximum adsorption of only 11.9 % for $[PdCl_4]^{2-}$ and 10.0 % for $[PtCl_4]^{2-}$ was obtained from the aqueous phase containing these metals in 0.5 M HCl solutions.
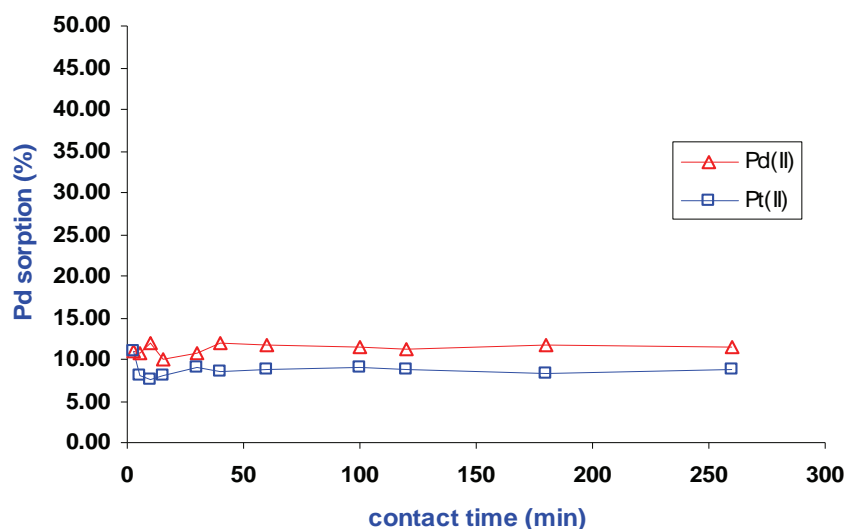
Figure 17. Effect of contact time on the adsorption of anionic Pd(II) and Pt(II) complexes from 0.5 M HCl onto FeSiAPTS. Experimental conditions: mass FeSiAPTS used: 10 mg; Pd(II) concentration used: 7.7 mg/L; Pt(II) concentration used: 10.0 mg/L. Total metal aqueous phase: 10 mL; pH: 0.26; Temperature: 21 ± 1 ºC.

However, when the pH of the aqueous solution containing HCl is increased to 2.27 (HCl concentration 0.01M), significant improvement in adsorption efficiency of $[PdCl_4]^{2-}$ and $[PtCl_4]^{2-}$ using **(1)** is observed, as shown in *Figure 18*. Interestingly, the rate at which these precious metals were adsorbed is rapid with the adsorption equilibrium being reached in 35 minutes.
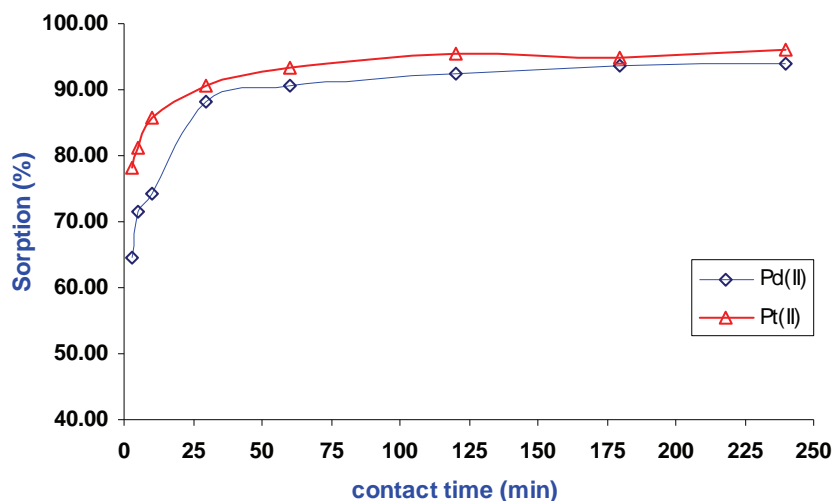
Figure 18. Effect of contact time on the adsorption of Pd(II) and Pt(II) onto FeSiAPTS. Single-metal solution experiments in 0.01 M HCl. Experimental conditions: mass FeSiAPTS used: 10 mg; Pd(II) concentration used: 7.8 mg/L; Pt(II) concentration used: 9.8 mg/L; Total metal aqueous phase: 10 mL; pH: 2.27; Temp: 21 ± 1 ºC.

It is evident from the high initial slope and good adsorption efficiency that material (**1**) in fact has a high affinity for these precious metals. It was found that after only 3 minutes of contact, 78.2 % $[PtCl_4]^{2-}$ has been adsorbed whereas up to 64.6 % $[PdCl_4]^{2-}$ metal species has been adsorbed. Overall, at equilibrium a maximum adsorption of 95.9 % $[PdCl_4]^{2-}$ and 98.8 % $[PtCl_4]^{2-}$ was obtained. Thus, decreasing the molarity of the aqueous acidic solutions were accompanied by an improvement in the rate of $[PdCl_4]^{2-}$ and $[PtCl_4]^{2-}$ adsorption when compared to experiments conducted in 0.5 M HCl solutions (*Figure 17*). From these results, it could therefore be concluded that the solution pH and the concentration of free unbound Cl⁻ ions have an influence on the adsorption and removal of these metal species from the solutions using material (**1**).

4.1.1.2 Effect of contact time on [AuCl₄]⁻ adsorption

The effect of contact time on the adsorption of $[AuCl_4]^-$ was also investigated in order to determine the rate of sorption using different quantities of both materials (**1**) and (**2**). The results obtained for the $[AuCl_4]^-$ single-metal solution experiments are presented in *Figure 19*. The experimental conditions that were used are given in the figure captions. It should be noted that in these particular experiments, a constant HCl solution concentration of 0.5 M was used (pH < 1).

The amount of gold adsorbed (as mass %) as a function of contact time is shown in *Figures 19 (a)* and *(b)* for different quantities (10, 30, and 50 mg) of (**1**) and (**2**), respectively. It was

the dependence of the sorption kinetics on the quantity of (**1**) and (**2**), suggests that an additional mechanism (other then ion-exchange) is likely to be responsible for the adsorption of $[AuCl_4]^-$ onto the studied materials. It is evident though that $[AuCl_4]^-$ is not effectively absorbed by (**1**) and (**2**) under the studied experimental conditions.
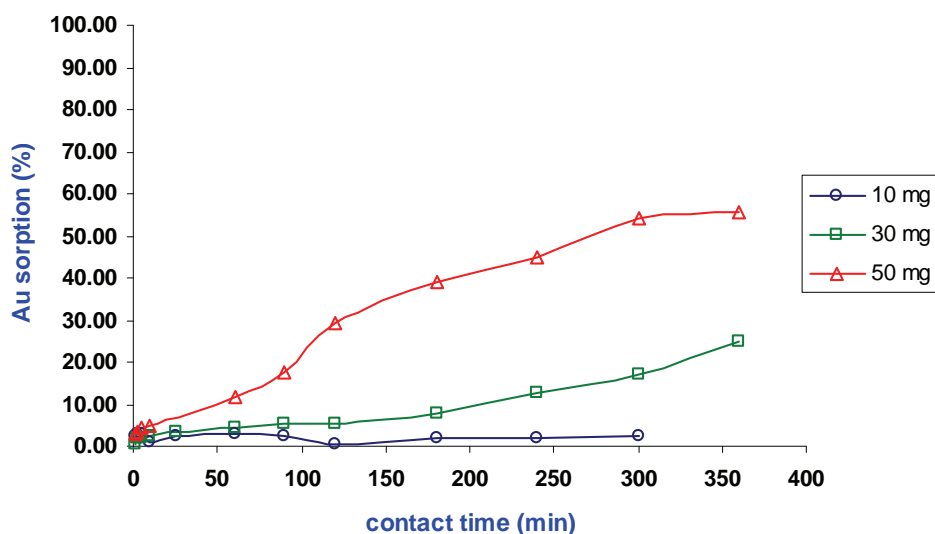

*Figure 19 (a). Effect of contact time on the adsorption of Au(III) by (**1**) FeSiAPTS. Single-metal experiment done in 0.5 M HCl. Experimental conditions: masses material used: 10, 30, 50 mg; constant Au(III) concentration: 20 mg/L; Total metal aqueous phase: 10 mL; Temp: 21 ± 1ºC.*
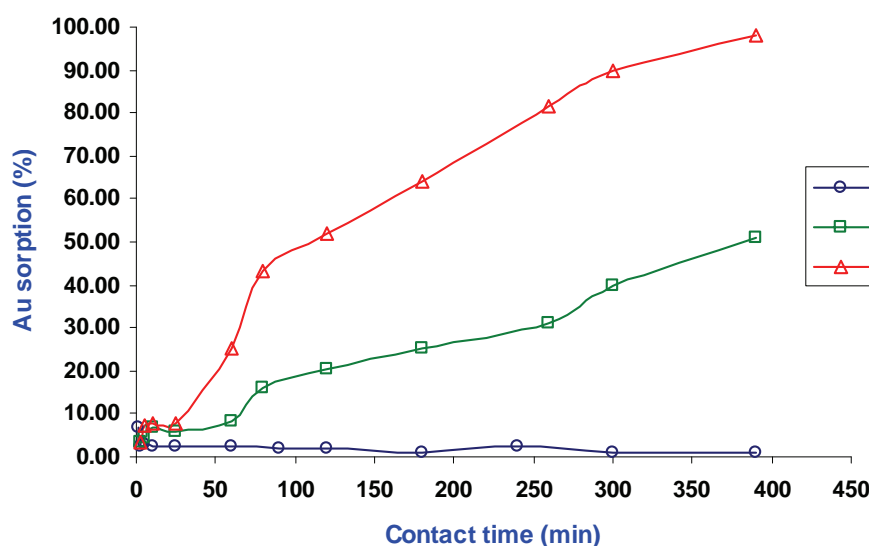

*Figure 19 (b). Effect of contact time on the adsorption of Au(III) by (**2**) FeSiED. Single-metal experiment done in 0.5 M HCl. Experimental conditions: masses material used: 10, 30, 50 mg; constant Au(III) concentration: 20 mg/L; Total metal aqueous phase: 10 mL; Temp: 21 ± 1ºC.*

_____

As in the case of the PGM adsorption from solution (*Figure 18*) using material (**1**), [AuCl$_4$]$^-$ adsorption efficiency improved with a decrease in the aqueous HCl concentrations from 0.5 M to 0.01M (*Figure 20*). The rate of adsorption was relatively fast. After only 3 minutes, almost 52 % of the [AuCl$_4$]$^-$ species in solution is adsorbed and in less than 30 minutes equilibrium adsorption is reached. At equilibrium, a maximum equilibrium adsorption of 76.8 % is observed. It is evident from the high initial slope and good adsorption efficiency that material (**1**) has a high affinity for [AuCl$_4$]$^-$ in 0.01 M HCl as compared to the adsorption from 0.5 M HCl.
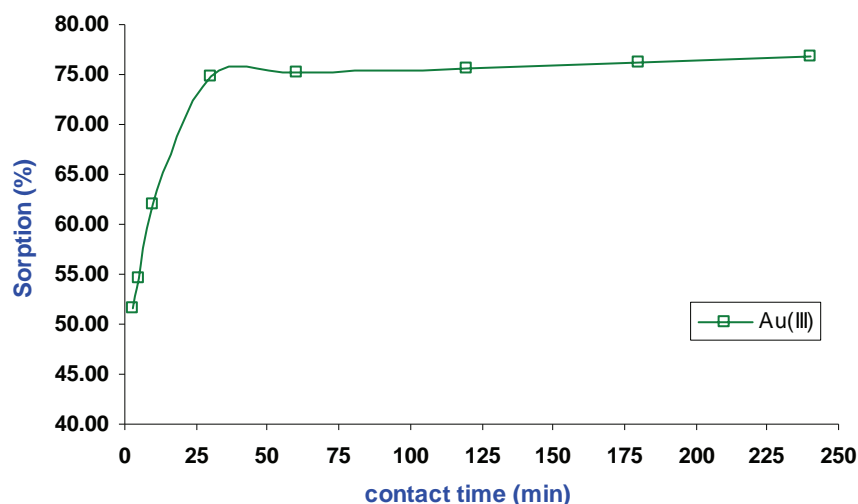

Figure 20. Effect of contact time on the adsorption of Au(III) onto FeSiAPTS. Single-metal solution experiments in 0.01 M HCl. Experimental conditions: mass FeSiAPTS used: 10 mg; Pd(II) concentration used: 7.8 mg/L; Pt(II) concentration used: 9.8 mg/L; Total metal aqueous phase: 10 mL; pH: 2.27; Temp: 21 ± 1 ºC.

As already alluded to, in HCl media, platinum, palladium and gold readily form chloro-complexes, whose distribution strongly depends on solution pH and chloride concentration.[126] It has been reported that in aqueous acidic solutions with chloride concentration above 5 mM, Pt(II), Pd(II) and Au(III) are present in solution only in the form of chloro-platinate, chloro-palladate, and chloro-auric complexes with anionic charges. In solutions with chloride concentrations between 0.7 – 5 mM, these complexes normally have neutral charges and in solutions with lower chloride concentrations (below 0.7 mM) they have cationic charges.[127]
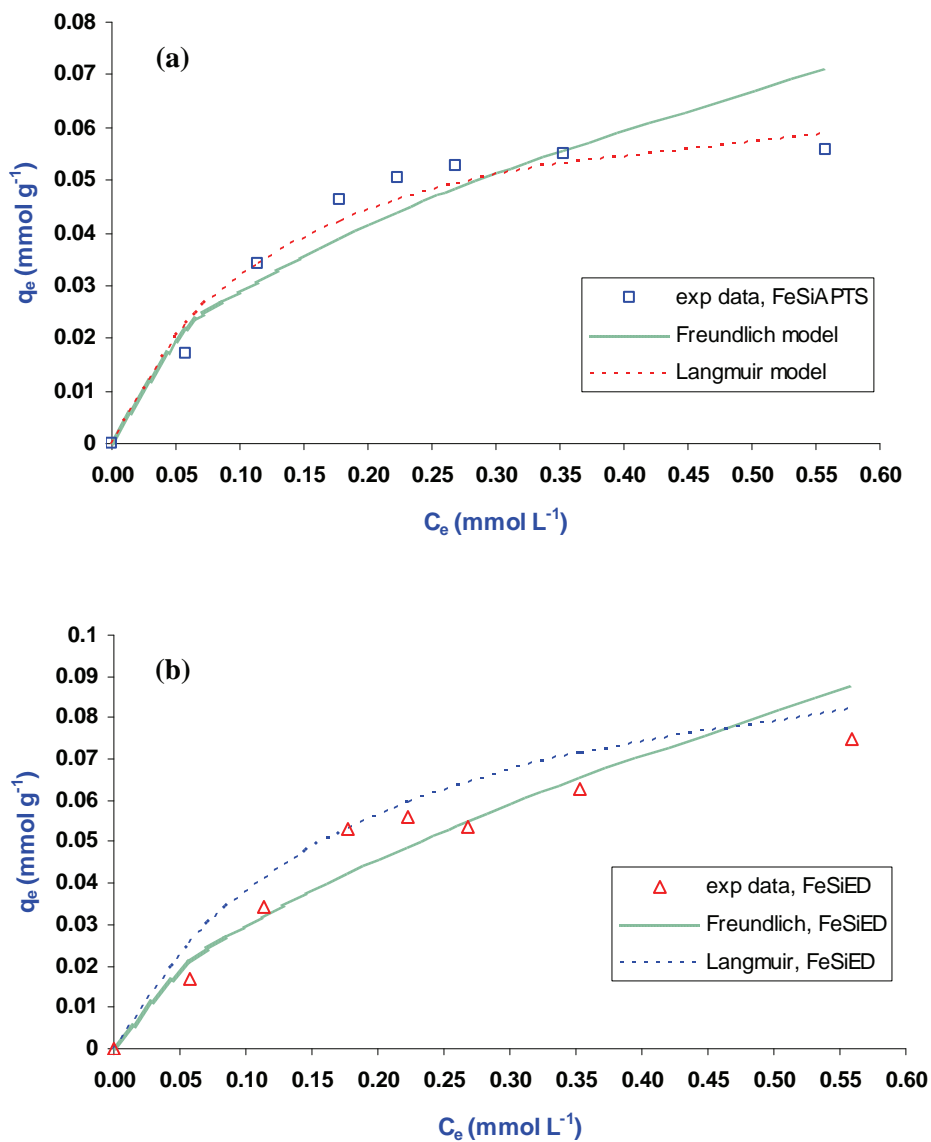
Figure 21. The relationship between the equilibrium loading capacity and the equilibrium gold concentration for (a) FeSiAPTS and (b) FeSiED. Experimental conditions: mass material used: 50 mg; contact time: 24 h, total metal aqueous phase: 15 mL, hydrochloric acid concentration: 0.5 M; temperature: 21 ± 1ºC.
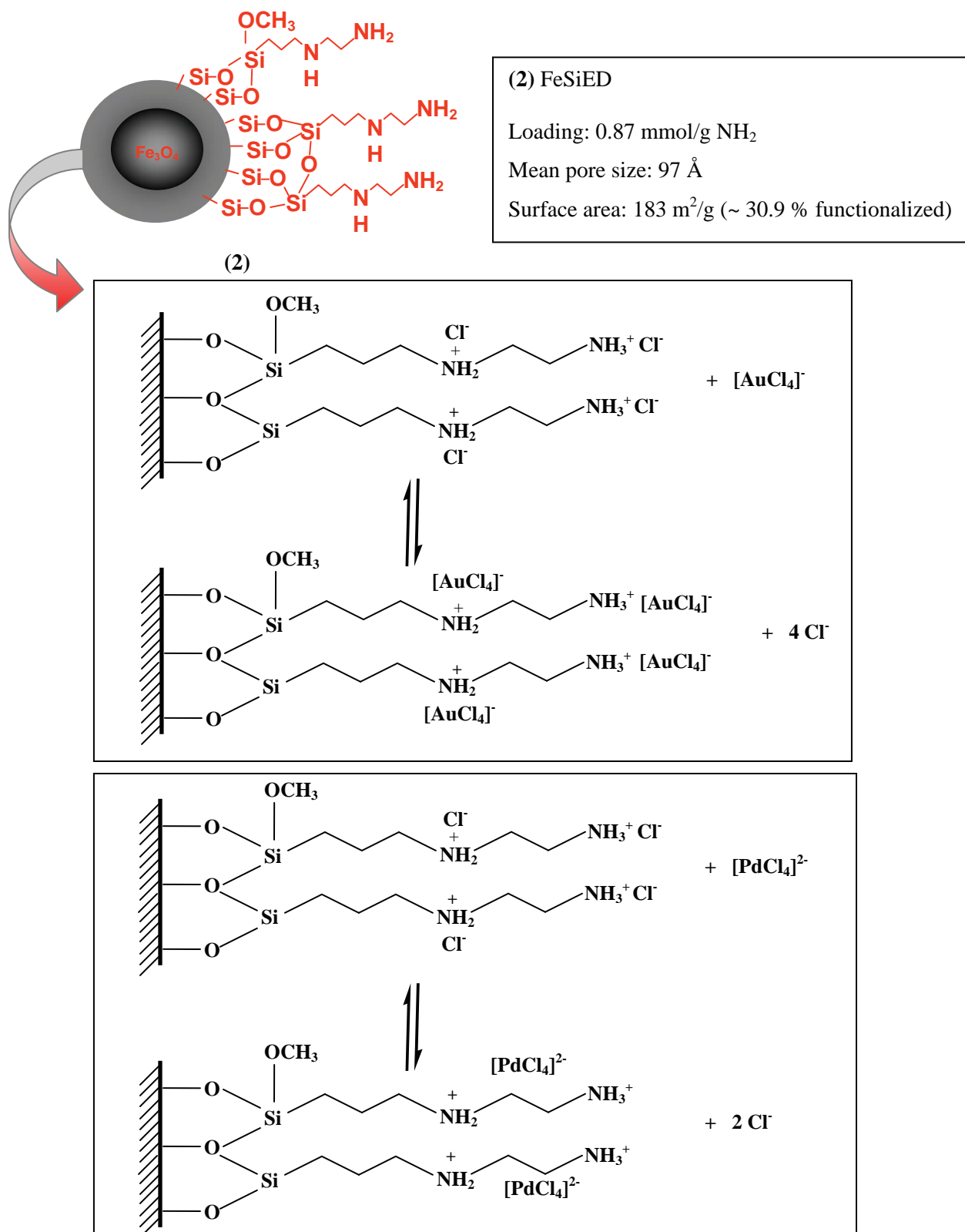
one data point) was 0.5 M plus the additional amounts added. It should be noted that only this additional amounts of chloride ions added is given on the x-axis in *Figure 22*. Recall from our previous study (*Figure 19*), adsorption equilibrium was not reached after 360 minutes. Therefore, a longer contact time of 24 h was utilized in these experiments, in order to ensure that equilibrium was approached.

The logarithm of the distribution coefficients and sorption capacity of $[AuCl_4]^-$ as a function of free chloride ions in solution is shown in *Figure 22*. As can be seen, *Figure 22* demonstrates that the chloride ions interfered with the $[AuCl_4]^-$ adsorption as shown by the decrease in sorption capacity and distribution coefficients K with increasing molar solutions of chloride ions. This decrease of $[AuCl_4]^-$ sorption with increasing concentration of counter ions (Cl^-) can be explained by the competition between the $[AuCl_4]^-$ chloro-complexes and the chloride anions, which may interact with the protonated amine groups of the adsorbent materials. This confirmed that the electrostatic attraction *via* ion-exchange was a likely mechanism responsible for the adsorption of $[AuCl_4]^-$ on protonated amine groups. Furthermore, as expected and as can be seen, the loading capacity of (**2**) FeSiED, was generally higher than that of resin (**1**) FeSiAPTS, due to the relatively higher degree of amine functionality and thus higher ligand concentration in the backbone of resin (**2**) (*refer to chapter 3*).
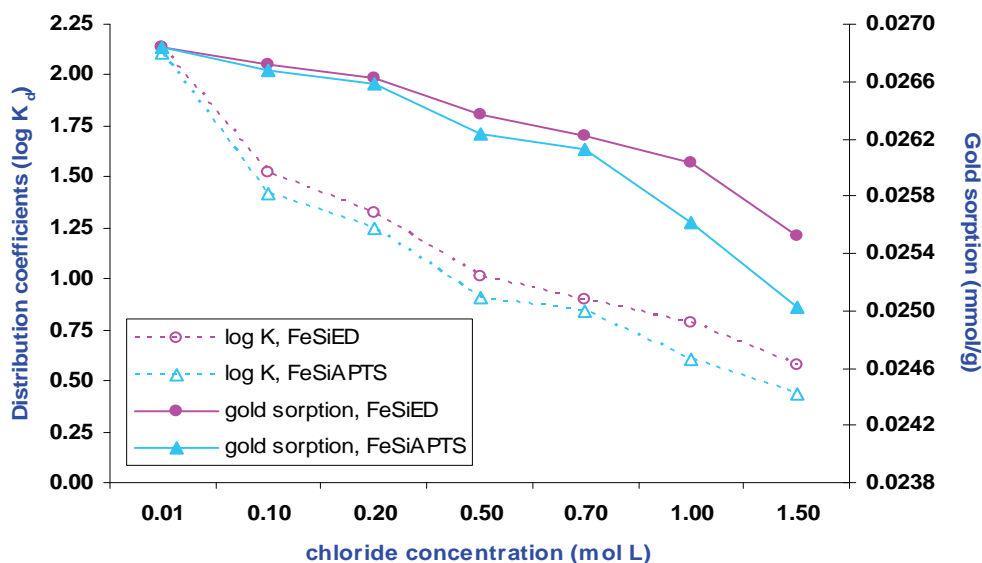
*Figure 22. The effect of chloride ion concentration on the adsorption of Au(III) from aqueous acidic solutions onto (**1**) FeSiAPTS and (**2**) FeSiED. Experimental conditions: mass FeSiAPTS and FeSiED used: 50 mg; Au(III) concentration used: 26 mg/L in 0.5 M HCl. Total metal aqueous phase: 10 mL; additional chloride ion aqueous phase: 10 mL; Temperature: 21 ± 1 ºC.*

(1) FeSiAPTS

Loading: 0.75 mmol/g NH_2

Mean pore size: 97 Å

Surface area: 183 m^2/g (~ 27 % functionalized)

Scheme 10. Mechanism of $[AuCl_4]^-$ and $[PdCl_4]^{2-}$ removal from acidic solutions by FeSiAPTS.

(2) FeSiED

Loading: 0.87 mmol/g NH$_2$

Mean pore size: 97 Å

Surface area: 183 m^2/g (~ 30.9 % functionalized)

Scheme 11. Mechanism of [AuCl$_4$]$^-$ and [PdCl$_4$]$^{2-}$ removal from acidic solutions by FeSiED.

4.1.2 Preliminary study to investigate [AuCl$_4$]$^-$, [PdCl$_4$]$^{2-}$ and [PdCl$_4$]$^{2-}$ recovery from solution

In a preliminary study as shown by the results in *Figure 23*, it was found that after 24 h contact, [PdCl$_4$]$^{2-}$ and [PtCl$_4$]$^{2-}$ was efficiently removed from aqueous acidic solutions by amine functionalized silica-coated SPMNs, FeSiAPTS and FeSiDETA. The good adsorption efficiency are attributed to an ion-exchange mechanism as shown in *Scheme 10 and 11*, since these materials is essentially protonated in solution and would readily facilitate these processes. As can be seen, the adsorption efficiency of [PdCl$_4$]$^{2-}$ and [PtCl$_4$]$^{2-}$ by unfunctionalized SPMNs (Fe$_3$O$_4$) and silica-coated SPMNs (FeSi) is lower. The mechanism responsible for these adsorption processes most likely entails electrostatic interactions between protonated surface hydroxyl groups and the anionic complexes. Surprisingly, it is found that [AuCl$_4$]$^-$ was consistently removed not only by the amine-functionalized silica-coated SPMNs but also the unfunctionalized SPMNs. The [AuCl$_4$]$^-$ species was quantitatively adsorbed. From these results it is apparent that surface silica coating and amine functionalization is not necessary to efficiently remove [AuCl$_4$]$^-$ from dilute HCl solutions. For this reason, we became interested in studying the [AuCl$_4$]$^-$ removal from aqueous acidic solutions by using in particular unfunctionalized SPMNs. The results of these studies are reported in *Chapter 5*.
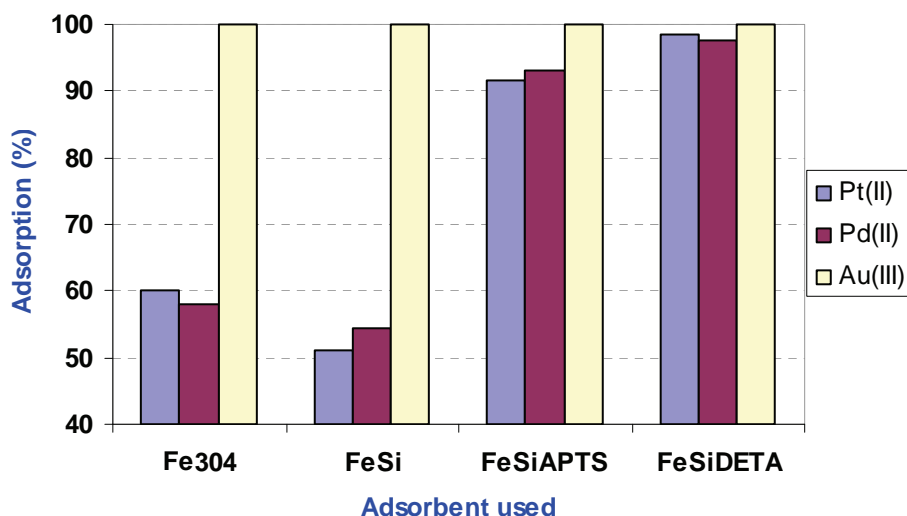

Figure 23. Adsorption of Au(III), Pd(II) and Pt(II) from 0.1 M HCl by various adsorbent materials. Experimental conditions: mass FeSiAPTS used: 50 mg; Au(III) concentration: 19.1 mg/L; Pd(II) concentration used: 10.8 mg/L; Pt(II) concentration used: 12.2 mg/L; Total metal aqueous phase: 15 mL; Temp: 21 ± 1 ºC.
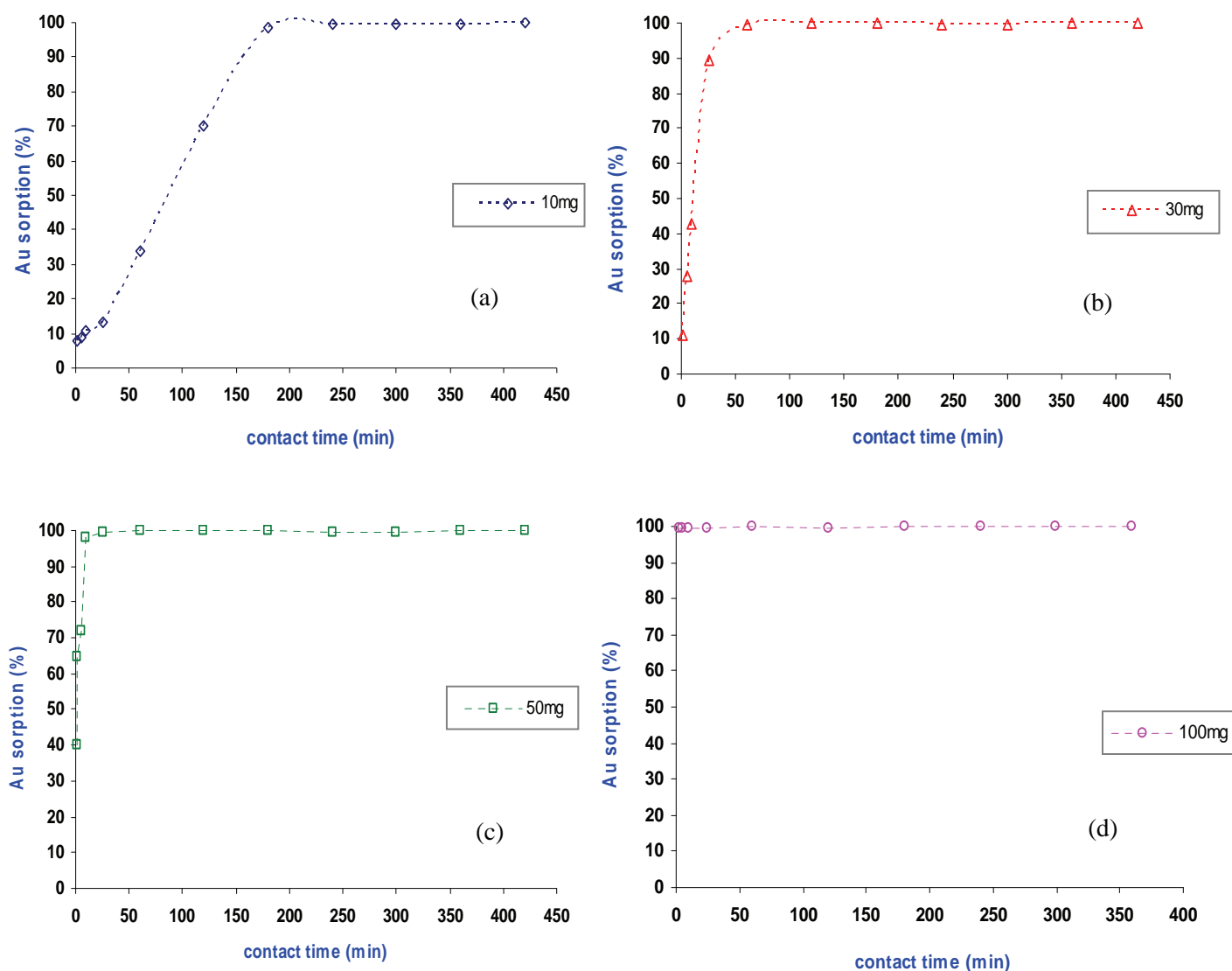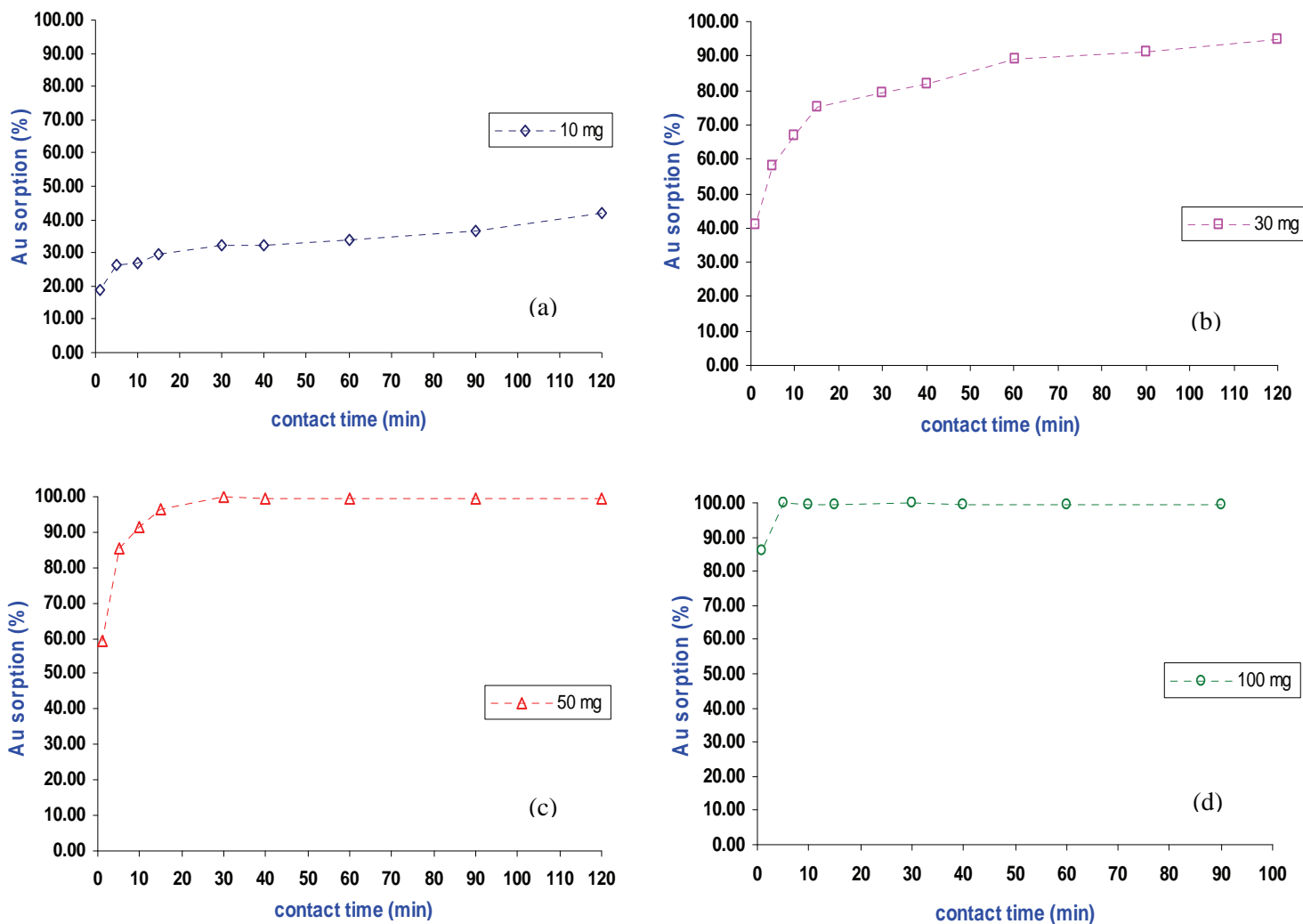
_____

Figure 24. Effect of contact time on the adsorption of Au(III) onto SPMNs. Single-metal solution experiments in 0.5 M HCl. Experimental conditions: mass SPMNs used: (a) 10 mg, (b) 30 mg, (c) 50 mg, (d) 100 mg; Au(III) concentration used: 20.5 mg/L; Total metal aqueous phase: 10 mL; Temperature: 21 ± 1ºC. Each experimental data point represents one sorption experiment.

As could be seen from *Figure 24 (a – d)*, with increasing the mass of the SPMNs in the individual batch experiments from 10 to 100 mg samples, the rate of adsorption increased, with 50 % of the total "available" $[AuCl_4]^-$ in solution ($t_{1/2}$) being reached in less than 90 minutes for the 10 mg batch experiment (*Figure 24 a*), less than 10 minutes for the 30 mg batch experiment (*Figure 24 b*) and less than 5 minutes for the 50 mg batch experiments (*Figure 24 c*). In the case of the 100 mg batch experiment the rate of $[AuCl_4]^-$ sorption was extremely rapid (*Figure 24 d*).

The rate at which $[AuCl_4]^-$ is adsorbed by SPMNs from 0.01 M HCl solutions was also investigated. In this regard, a series of $[AuCl_4]^-$ batch sorption experiments were carried out for different masses (10, 30, 50, 100 mg) following the same experimental methodology as used in the 0.5 M HCl experiments. The results obtained for the adsorption of $[AuCl_4]^-$ from 0.01 M HCl as a function of contact time are shown in *Figure 25*.

Figure 25. Effect of contact time on the adsorption of Au(III) onto SPMNs. Single-metal solution experiments in 0.01 M HCl. Experimental conditions: mass SPMNs used: (a) 10 mg, (b) 30 mg, (c) 50 mg, (d) 100 mg; Au(III) concentration used: 20.1 mg/L; Total metal aqueous phase: 10 mL; Temperature: 21 ± 1ºC. Each experimental data point represents one sorption experiment.

_____

5.1.1.2 Effect of initial [AuCl$_4$]$^-$ concentration on adsorption by unfunctionalized SPMNs

The effect of various [AuCl$_4$]$^-$ concentrations in solution on the adsorption of SPMNs was investigated in order to estimate the maximum loading capacity of the SPMNs. The results of the relationship between the equilibrium [AuCl$_4$]$^-$ concentration in the aqueous phase, C$_e$, and the equilibrium loading capacity, q$_e$, is shown in *Figure 26*. As seen from the results, the equilibrium load of [AuCl$_4$]$^-$ (mmol) per unit mass (g) of material increased almost linearly upon increasing the initial concentration of [AuCl$_4$]$^-$ species in solution up to *ca* 0.26 mmol/L and then no significant change was observed as equilibrium was approached. The maximum experimental equilibrium loading capacity was found to be 0.051 mmol [AuCl$_4$]$^-$ loaded per gram of SPMN material. As was done previously, the experimental data were fitted to non-competitive *Langmuir* and *Freundlich models*. However, only the experimental data fitted to the Langmuir model is presented here. The data fitted to the *Freundlich model* is omitted. It was found that there was not a good applicability between the data and the latter model. The fitting of the experimental data to the Langmuir model is given in *Figure 26*. As was expected by applying the model, a plot of C$_e$/q$_e$ against C$_e$ resulted in a straight line from which the Langmuir parameters could be obtained. Using the model, a theoretical value of the maximum equilibrium loading capacity, q$_e$, was calculated to be 0.071 mmol/g (13.984 mg/g). The experimental data was in reasonable good agreement with the *Langmuir* adsorption model, which indicates monolayer coverage on the SPMN surface.
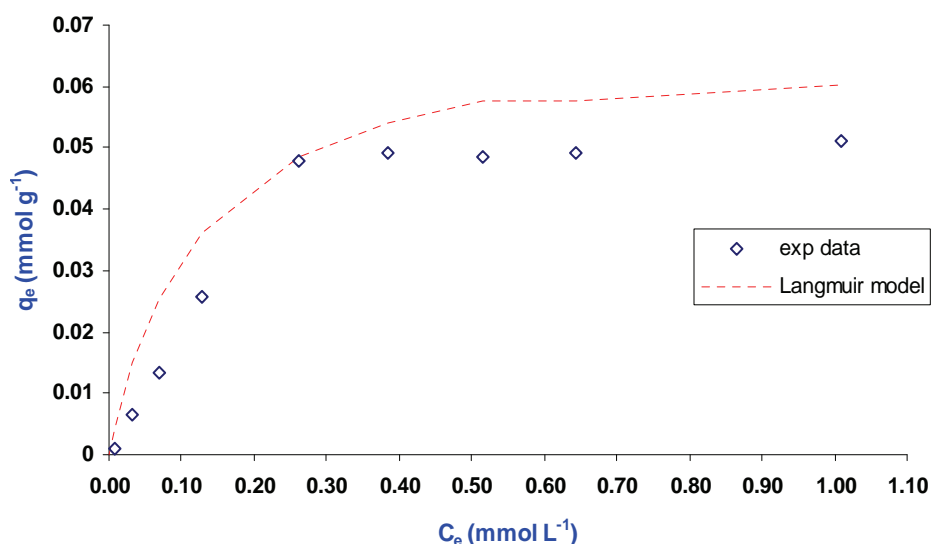

Figure 26. The relationship between the equilibrium loading capacity and the equilibrium gold concentration for SPMNs. Experimental conditions: mass material used: 50 mg; contact time: 60 minutes, total metal aqueous phase: 10 mL, hydrochloric acid concentration: 0.5 M; temperature: 21 $\pm$ 1ºC.

_____

5.1.2 Adsorption of $[PdCl_4]^{2-}$ and $[PtCl_4]^{2-}$ using unfunctionalized SPMNs

5.1.2.1 Effect of contact time on $[PdCl_4]^{2-}$ and $[PtCl_4]^{2-}$ adsorption

The effect of contact time on the adsorption of $[PdCl_4]^{2-}$ and $[PtCl_4]^{2-}$ species from 0.5 M HCl and 0.01 M HCl using the SPMNs as adsorbent materials was also investigated. Once again, the experimental conditions were similar to those used in the $[AuCl_4]^-$ batch sorption studies. The results obtained from the batch experiments conducted in 0.5 M HCl are presented in *Figure 27*. It was evident that under the experimental conditions, SPMNs show low affinity towards these PGMs. Results indicates that the adsorption was almost negligible, with the sorption percentage not exceeding 6 % for $[PtCl_4]^{2-}$ and 3 % for $[PdCl_4]^{2-}$ species. Increasing the mass of the SPMNs in the batch experiments up to the 100 mg sample had no significant effect on the sorption efficiency. Therefore, only the 50 mg batch experiment results are shown. Similar trends were observed when conducting the same experiments in 0.1 M HCl solutions as shown in *Figure 28*. However, there was an increase in the adsorption efficiency. The results (*Figure 28*) show that sorption percentage did not exceed 13 % for the $[PtCl_4]^{2-}$ and 10 % for the $[PdCl_4]^{2-}$ species.
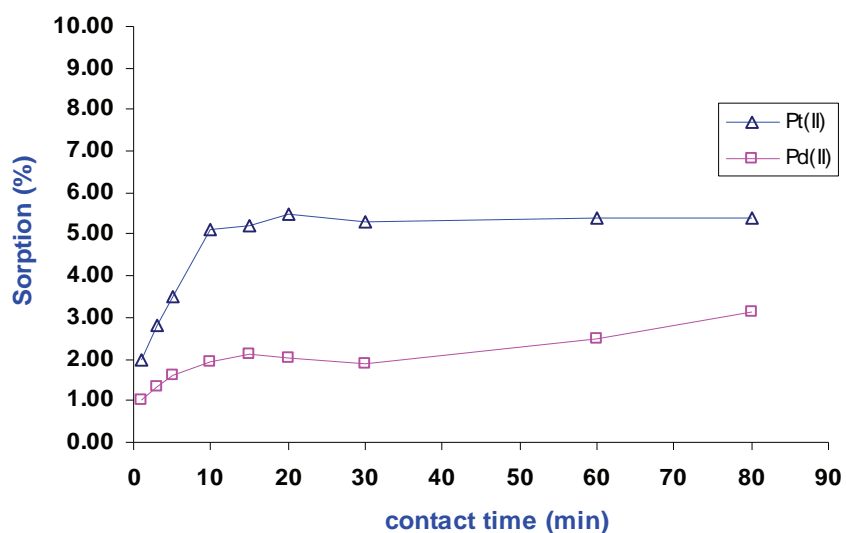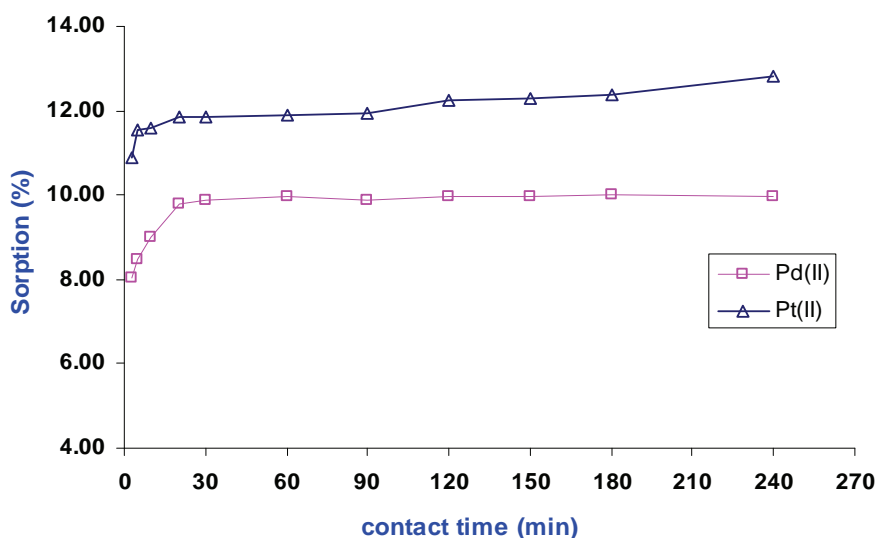

Figure 27. Effect of contact time on the adsorption of Pt(II) and Pd(II) onto SPMNs. Single-metal solution experiments in 0.5 M HCl. Experimental conditions: mass SPMNs used: 50 mg; Pt(II) concentration: 10 mg/L; Pd(II) concentration used: 7.7 mg/L; Total metal aqueous phase: 10 mL; Temperature: 21 ± 1°C. Each experimental data point represents one sorption experiment.

_____

Figure 28. Effect of contact time on the adsorption of Pt(II) and Pd(II) onto SPMNs. Single-metal solution experiments in 0.1 M HCl. Experimental conditions: mass SPMNs used: 50 mg; Pt(II) concentration: 9.70 mg/L; Pd(II) concentration used: 8.90 mg/L; Total metal aqueous phase: 10 mL; Temperature: 21 ± 1ºC. Each experimental data point represents one sorption experiment.

Next, the influence of different solution pH on the adsorption processes and the removal of $[PdCl_4]^{2-}$ and $[PtCl_4]^{2-}$ species from solution was investigated. The fact that SPMNs are unstable in solutions of high acidic content [42] was taken into account. Therefore, if the pH of the solutions containing the precious metals is too low, degradation due to iron dissolution might occur (*Section 4.3.2*). It was suspected that this would have a direct bearing on the adsorption processes, since the surface properties of the SPMNs will be altered. However, if the pH of the aqueous solution was too high, then hydrolysis of the precious metals could also occur. $[PdCl_4]^{2-}$ and $[PtCl_4]^{2-}$ are sensitive to hydrolysis and this will influence the distribution of the species in solution, and more specifically the formation of chloro-anionic complexes. In this regard, these experiments were done to determine the optimum pH range in which $[PdCl_4]^{2-}$ and $[PtCl_4]^{2-}$ could be most efficiently removed from solution and subsequently adsorbed by the unfunctionalized SPMNs. The aqueous solutions of different HCl concentrations (varying pH) that were used for these batch sorption experiments are as follows: 0.5 M HCl, 0.1 M HCl, 0.01 M HCl and 0.001 M HCl, respectively. In these pH ranges, $[PdCl_4]^{2-}$ and $[PtCl_4]^{2-}$ speciation is largely confined to the chloro-anionic complexes and metal cations.[126,127] The results obtained for the $[PdCl_4]^{2-}$ and $[PdCl_4]^{2-}$ adsorption from the different acid media are shown in *Figure 29*. The results obtained from the various acid media indicate that the adsorption of $[PdCl_4]^{2-}$ and $[PtCl_4]^{2-}$ by the SPMNs is strongly affected by solution pH. As can be seen from *Figure 29*, there is definite improvement

_____

in $[PdCl_4]^{2-}$ and $[PtCl_4]^{2-}$ adsorption efficiency with increasing solution pH. Thus, it is evident that the acidic content of the solutions has an influence on the adsorption of $[PdCl_4]^{2-}$ and $[PtCl_4]^{2-}$ by the SPMNs. Moreover, from *Figure 29 (a) and (b)* it can be seen that the sorption efficiency is also dependant on the masses of SPMNs. With an increase in the masses of SPMNs from 10 mg to 100 mg samples, the extent of $[PdCl_4]^{2-}$ and $[PtCl_4]^{2-}$ adsorption was drastically enhanced. From these results, it can be concluded that 0.001 M HCl solutions (pH 3) and SPMN mass exceeding 50 mg would suffice for quantitative $[PdCl_4]^{2-}$ and $[PtCl_4]^{2-}$ removal and adsorption.
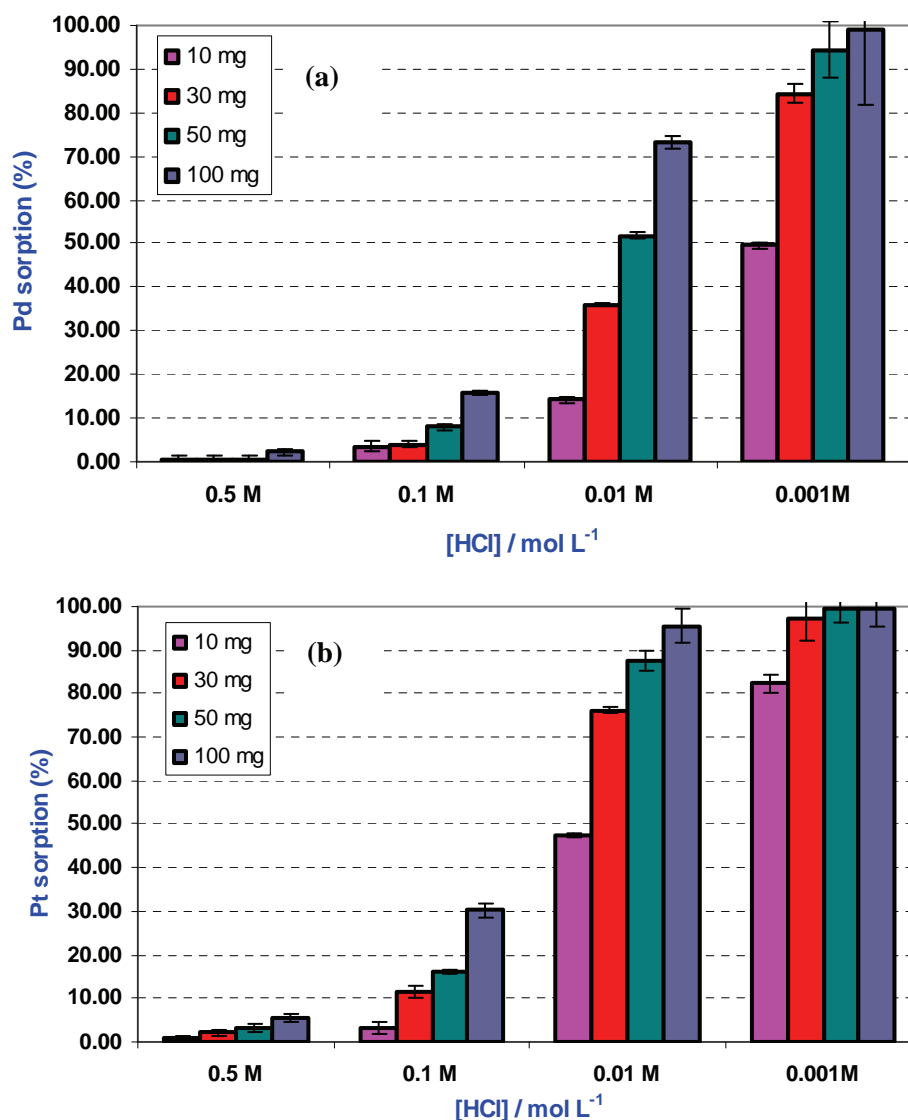

Figure 29. Effect of hydrochloric acid solution concentration (different solution pH) on the adsorption of (a) Pd(II) and (b) Pt(II) onto different quantities of SPMNs. Single-metal solution experiments. Experimental conditions: mass SPMNs used: 10, 30, 50, 100 mg; Pt(II) concentration range: 11.9 – 14.8 mg/L; Pd(II) concentration range: 7.0 – 10.6 mg/L; Total metal aqueous phase: 10 mL; contact time: 45 min. Temperature: 21 ± 1ºC.

_____

5.2 Investigation into the possible mechanism(s) responsible for the $[AuCl_4]^-$, $[PdCl_4]^{2-}$ and $[PtCl_4]^{2-}$ removal from solution using unfunctionalized SPMNs.

In this section, the possible mechanisms responsible for the removal of $[AuCl_4]^-$, $[PdCl_4]^{2-}$ and $[PtCl_4]^{2-}$ from acidic solutions are discussed. The objective of this study was to investigate whether adsorption was an efficient mechanism for the removal of these precious metals from aqueous acidic solutions. Here we will refer to SPMNs and Fe_3O_4 nanoparticles interchangeably.

### *5.2.1 Surface properties of SPMNs and the $[AuCl_4]^-$, $[PdCl_4]^{2-}$, $[PtCl_4]^{2-}$ interactions*

The iron oxide based SPMN surface have hydroxyl groups that can accept protons and could potentially take part in complexation reactions with certain metal ion species.[42] For the purpose of this discussion, the surface hydroxyl groups will be symbolized as $\equiv$Fe-OH. This convention is a simplification of the local structure at the SPMN surface. However, this relatively simple model of surface hydroxyl groups is assumed to be satisfactory for the modeling description of metal species adsorption.

The point of zero charge (PZC) of SPMNs is a relevant property that influences the adsorption ability of the $[AuCl_4]^-$, $[PdCl_4]^{2-}$ and $[PtCl_4]^{2-}$ species from acidic solutions onto these iron oxide materials. The PZC is the value of pH at which the adsorption of potential-determining ions on the iron oxide is zero.[42] The PZC for SPMNs has been reported to be in the range of 6.0 to 8.2.[42,133] At a pH less than the PZC, the $\equiv$Fe-OH$_2^+$ groups on the surface of the SPMNs predominate. Thus, under the experimental conditions used in these studies (solution pH < PZC), the SPMNs surface can be considered to be essentially protonated and positively charged, facilitating the adsorption of anionic metal complexes which is believed to take place *via* electrostatic interaction as illustrated by *Scheme 12*.
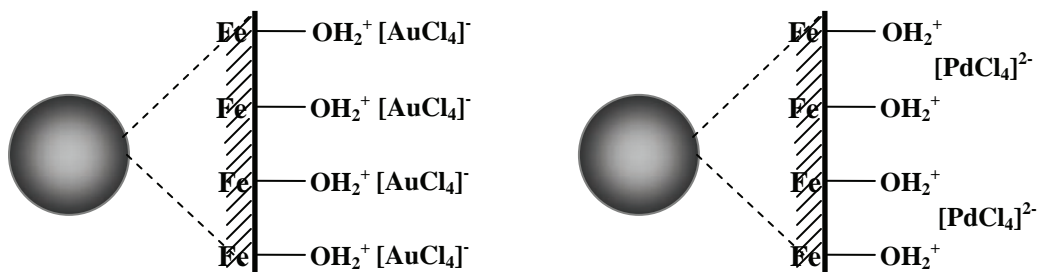
Scheme 12. Illustration of $[AuCl_4]^-$ and $[PdCl_4]^-$ species interaction with the protonated SPMNs surface sites. Note: only a section (not drawn to scale) of SPMN surface is shown.
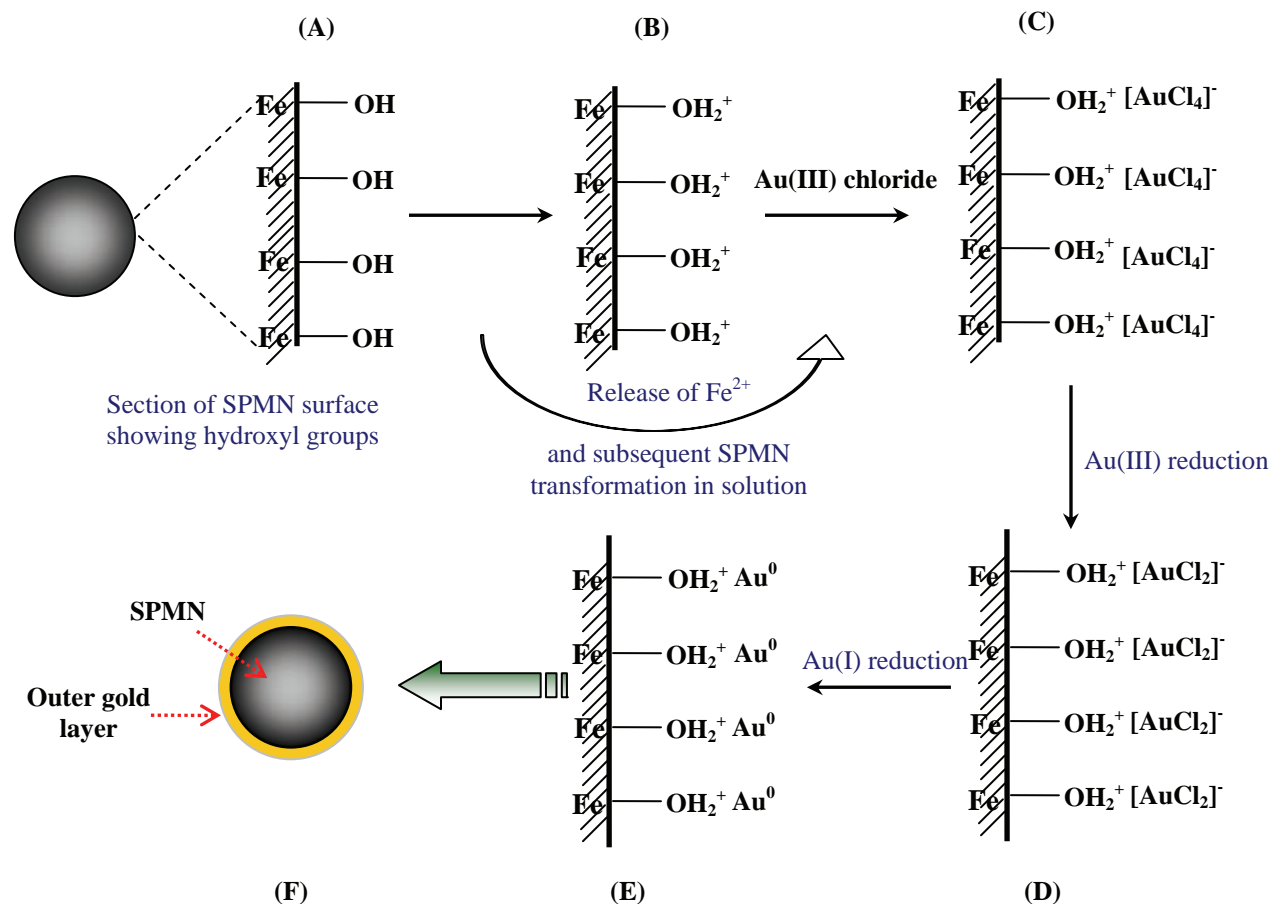
Scheme 13. Simultaneous dissolution, transformation, reduction and adsorption of gold from aqueous acidic solutions onto SPMN-iron oxide interface.

A - small section of SPMN surface illustrating surface hydroxyl groups

B - protonated SPMN surface sites ($\equiv$Fe-OH$_2^+$) as a result of acidic content of aqueous solutions containing the [AuCl$_4$]$^-$ anionic complexes. At this stage the dissolution and transformation processes are initiated.

**C -** electrostatic interaction between [AuCl$_4$]$^-$ anionic complexes and $\equiv$Fe-OH$_2^+$

D - electrostatic interaction between [AuCl$_2$]$^-$ anionic complexes and $\equiv$Fe-OH$_2^+$

E - electrostatic interaction between colloidal gold (Au^0) and $\equiv$Fe-OH$_2^+$

F - Formation of Au-enriched SPMN-iron oxide nanoparticles illustrating a gold coating around the SPMN-iron oxide nanoparticles.

_____

5.2.4 Effect of iron in solution on removal and adsorption of gold species

The effect of iron in solution (as a result of SPMN dissolution) on the amount of gold removed from aqueous solution and adsorbed by SPMNs was investigated. As for previous experiments, the solid SPMN phase was in contact with the aqueous phase containing a fixed, standard $[AuCl_4]^-$ concentration in 0.5 M HCl. After contact for the desired time periods ranging from 1 to 450 minutes, the solid phase was separated from the aqueous phase *via* magnetic sedimentation. The supernatant collected was then analyzed for gold as well as iron content by ICP-AES. From the analysis results obtained and using mass balance equations, the amount of gold loaded per gram of SPMN material was determined. The results obtained are shown in *Figure 30*, illustrating the amount of gold loaded as a function of free iron species in solution.
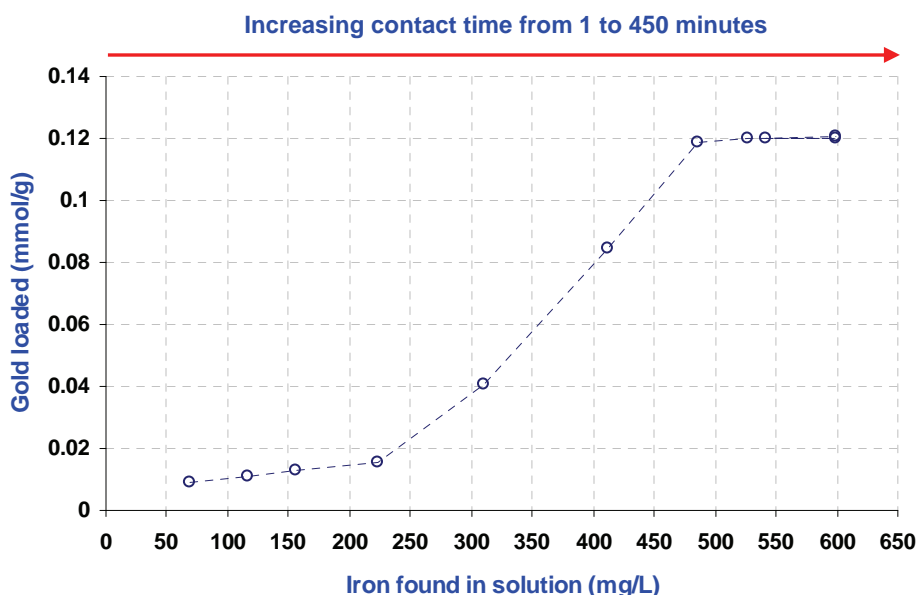

Figure 30. Effect of iron species in solution on the amount of gold loaded onto SPMNs. Single-metal solution experiment in 0.5 M HCl. Experimental conditions – SPMNs used: 10 mg; Au(III) concentration used: 20.5 mg/L; Total metal aqueous phase: 10 mL; Temperature: 21 ± 1ºC.

In this study it was assumed that the free iron in solution was mainly Fe^{2+} but it is likely that Fe^{3+} is also present in some quantity depending on the amount of dissolution and subsequent oxidation that occurred. We were not able to determine the oxidation states of these iron species in the solutions. It was only possible to determine the total amount (mg/L) of free iron species in solution as shown in *Figure 01*. As was already mentioned, it is energetically more favorable to release Fe^{2+} from the SPMN structure than the Fe^{3+} species.[42,67]

_____

5.2.5.1 Results of UV-Visible analysis of Au(III) species in 0.01 M HCl solution

The UV-Vis absorption spectrum of the tetrahedral $[AuCl_4]^-$ complex in 0.01 M HCl solution was collected and shown in *Figure 31*. The spectrum of this solution exhibits two absorption maxima at $\lambda = 229$ nm and $\lambda = 315$ nm as a result of the presence of $[AuCl_4]^-$ ions. The presence of these two absorption maxima enabled the recording of their changes with time, *i.e.* the concentration changes in the course of the reaction.
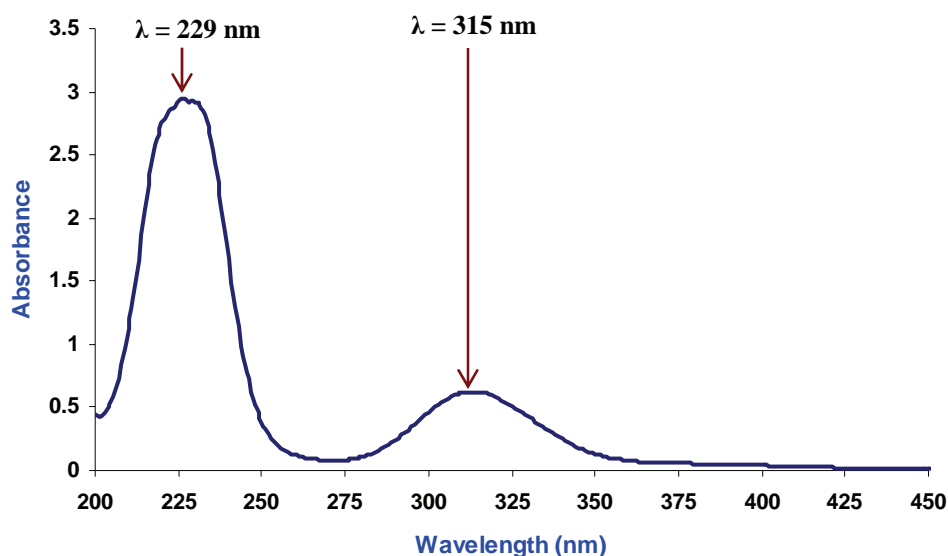
Figure 31. The UV-Vis absorption spectrum of feed solution containing 20 mg/L [AuCl₄]⁻ in 0.01 M HCl solution at ambient temperature. The absorption maxima are visible at λ = 229 nm and λ = 315 nm as a result of present [AuCl₄]⁻ ions. Experimental conditions: pH 0.43; temperature: 21 ± 1 ºC.

The absorption spectrum of $[AuCl_4]^-$ shown in *Figure 31* is essentially that of the feed solutions used during the sorption batch experiments as reported earlier. Spectrophotometric analysis was then also done on the effluents collected after the contact of aqueous phases containing $[AuCl_4]^-$ species in 0.01 M HCl with solid phases, SPMNs. The contact times in these experiments ranged from 2 – 90 minutes. The changes in the $[AuCl_4]^-$ absorption maxima with increasing contact times were monitored, taking into consideration that with increasing contact time more Fe^{2+} species are expected to be at the surface of the SPMN-iron oxide interface and also in solution. The results of these studies are shown in *Figure 32*. Each absorption spectrum shown in *Figure 32* represents the changes that occurred after the indicated contact times.
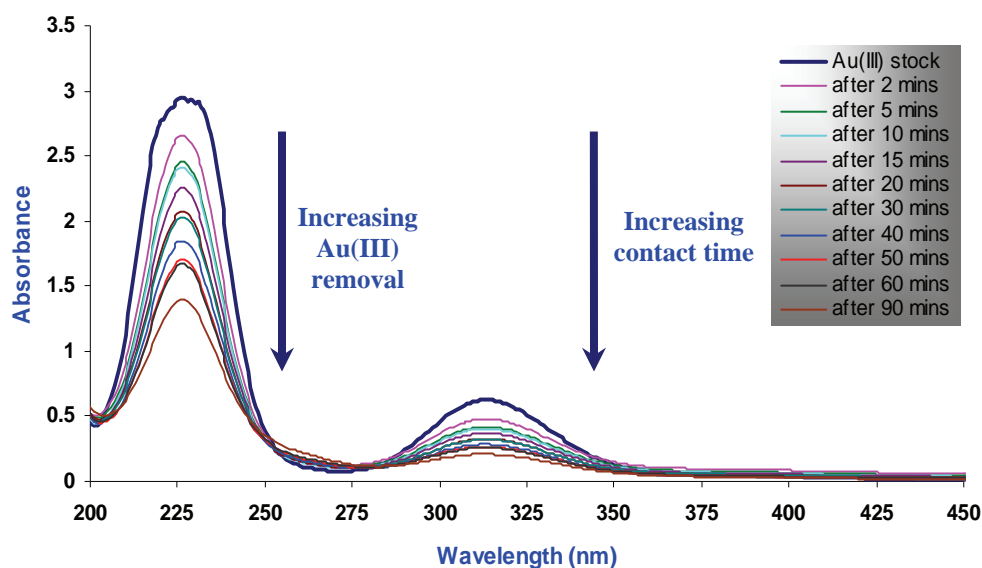
_____

Figure 32. The UV-Vis absorption spectra of gold species in 0.01 M HCl solution after various contact times. Experimental conditions - mass SPMNs used: 10 mg; contact times range: 2 – 90 minutes, total metal aqueous phase: 10 mL, HCl concentration: 0.01 M; temperature: 21 ± 1°C. The "bold" spectrum is that of the standard [AuCl₄]⁻ feed solutions.

As can be seen in *Figure 32*, in all cases the absorbance maxima at $\lambda = 229$ nm and $\lambda = 315$ nm decreased as a function of contact time, and this fact indicated decreasing $[AuCl_4]^-$ concentration in solution. This result was confirmed by ICP-AES as shown in *Figure 33*, demonstrating decreasing gold concentration in solution with increasing contact time.
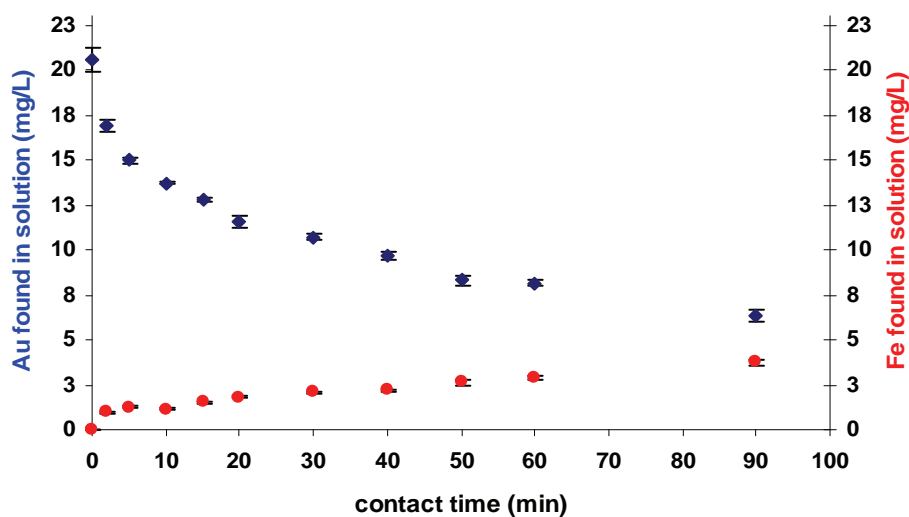

Figure 33. Amount of gold and iron left in solution with increasing contact time as determined from ICP-AES. The experimental conditions were same as for Figure 30.
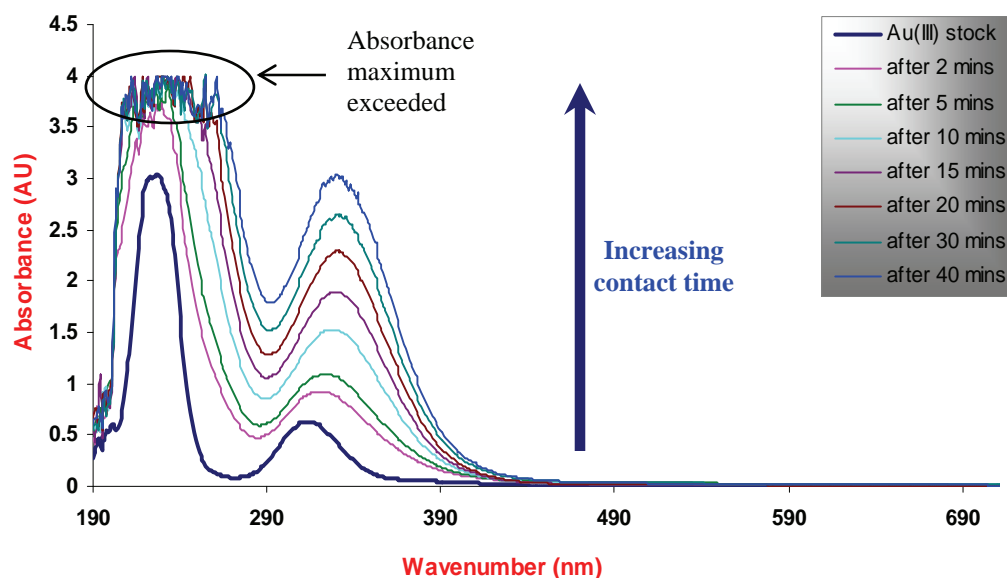
_____

Figure 34. UV-Vis absorption spectra of Au(III) in 0.5 M HCl solution after various contact times illustrating a shift in the absorption peaks. Experimental conditions - mass SPMNs used: 10 mg; contact times range: 2 – 40 minutes, total metal aqueous phase: 10 mL, HCl concentration: 0.5 M; temperature: 21 ± 1ºC. The "bold" spectrum is that of the standard [AuCl$_4$]$^-$ feed solutions.

In 0.5 M HCl there is a significant difference in the absorption spectra as compared to the absorption spectra in 0.01 M HCl (*Figure 32*). As can be seen in *Figure 34*, with increasing contact time there is an increase in the absorption maxima at $\lambda = 229$ and $\lambda = 315$ migrates to a higher wavelength at $\lambda = 334$, suggesting the formation of new species with higher molar absorptivity than [AuCl$_4$]$^-$ species. The increase and shift in absorbance in the UV-Vis can most likely be attributed to the formation of Fe^{III}Cl$_n^{(3-n)}$ species (for n = 3,4,5,6) as a result of increasing reduction of Au^{3+} to Au$^+$ with simultaneous oxidation of Fe^{2+} to Fe^{3+} species. Since there are excess amounts of Fe^{3+} and chloride ions in the solution, this was favorable for the formation of the iron(III) complex.

To confirm this, a series of UV-Vis experiments were performed to monitor the changes in the absorption maxima of a standard Fe^{3+} stock solution with similar concentrations as found in the effluents of the samples. The absorption spectrum of the Fe^{3+} stock solution is shown in *Figure 35*. The Fe^{3+} stock solution was prepared from the ferric salt, FeCl$_3$.6H$_2$O. Moreover, the same quantities of SPMNs were contacted for the same amount of time in 0.5 M HCl solutions (without the presence of gold in these solutions) and the changes in the absorption maxima intensity were monitored spectrophotometrically.

_____

The UV-Vis spectrum of the Fe^{3+} stock solution is shown in *Figure 35* and the changes in the absorption maxima for the SPMNs with time is shown in *Figure 36*.
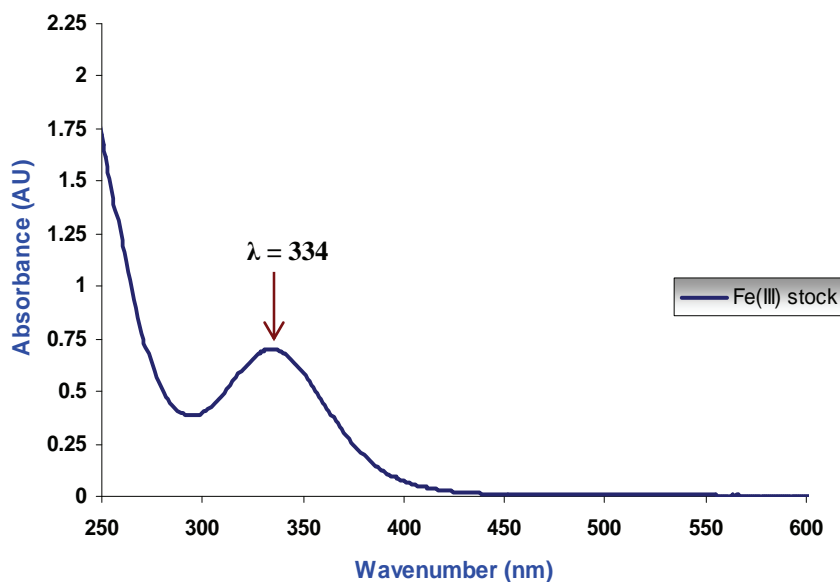

Figure 35. The UV-Vis absorption spectrum of Fe(III) stock solution in 0.5 M HCl solution. The absorption maxima is observed at λ = 334 nm.
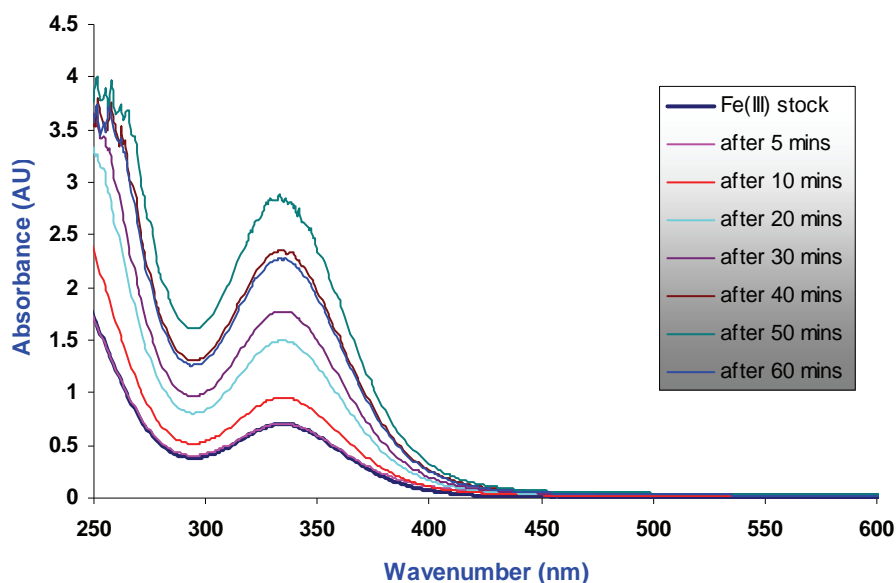

Figure 36. The UV-Vis absorption spectra of the formation of iron species in 0.5 M HCl solution after various contact times. Experimental conditions- mass SPMNs used: 10 mg; contact times range: as shown in figure legend, HCl concentration: 0.5 M; temperature: 21 ± 1ºC. The "bold" spectrum is that of the standard iron solutions.

89

_____

As can be seen from *Figure 36*, there is a significant increase in the absorption maxima at $\lambda = 334$ nm, which indicates the increasing formation of $Fe^{II}Cl_n^{(3-n)}$ species. This is in accordance with what was expected, since with increasing contact time more iron is present in solution. Therefore, from this result can be concluded that the increase in the absorption maxima intensity is due to the formation of $Fe^{III}Cl_n^{(3-n)}$ species, which in turn confirms the reduction mechanism as illustrated in *equations 21 – 23*.

5.2.6 Physical characterization of gold coated SPMNs.

Transmission electron microscopy (TEM) analysis was performed after a single preliminary sorption experiment to investigate whether gold was adsorbed onto the surface of SPMNs and to evaluate the gold-enriched SPMN morphology and size. In this regard, a known volume of a 23 mg/L $[AuCl_4]^-$ solution in 0.5 M HCl was in contact with the solid phase by agitation for 50 minutes. The solid phase was then separated from the aqueous phase by magnetic decantation and the effluent analyzed with TEM. It was found that gold was efficiently removed from the solution and almost quantitatively adsorbed by SPMNs. In *Figure 37* is shown the TEM micrograph depicting pseudo-trigonal shaped particles with average diameter of 12 ± 1.7 nm. The pseudo-trigonal particles are characteristic of colloidal gold.[139] These findings support the hypothesis of Au(III) reduction by the SPMNs to Au(0). However, since this was only a preliminary experiment it is necessary to conduct a more systematic study to conclusively proof the hypothesis by taking into account that poorly ordered iron oxide-SPMNs have a high affinity for gold species.
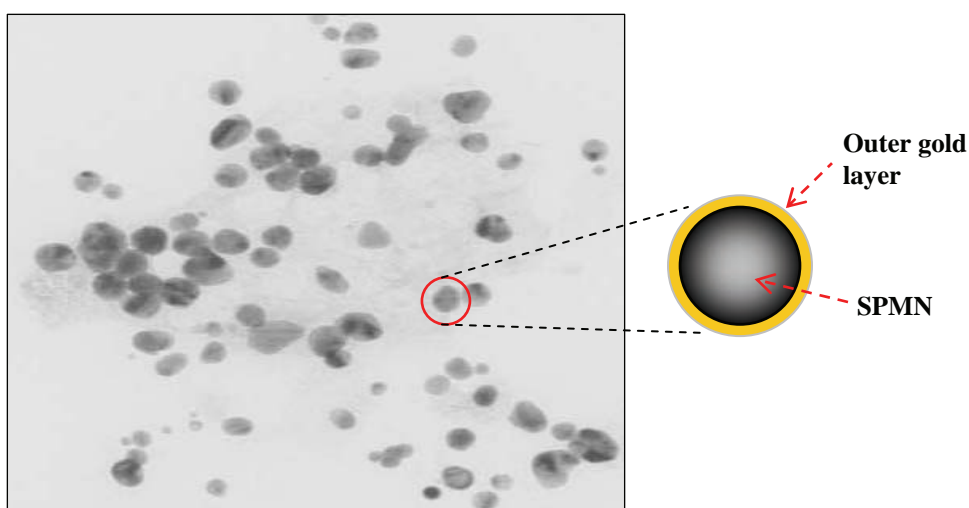
Figure 37. TEM images of the SPMNs after sorption of gold.

_____

The solid iron oxide – SPMN phase collected after the preliminary gold sorption experiment was dried under ambient conditions after separation from aqueous phase. Elemental composition analysis by energy Dispersive X-ray spectroscopy (EDX) was then done on this dried sample. The result is shown in *Figure 38* below.
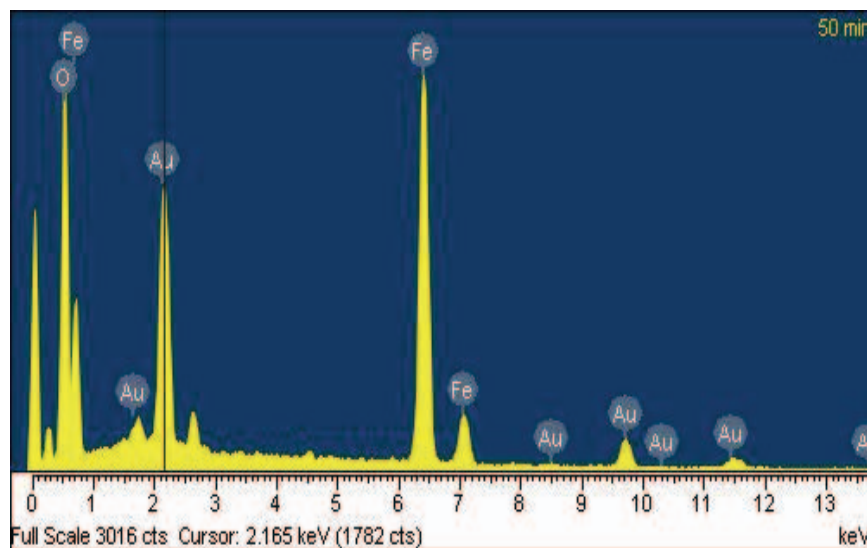

Figure 38. EDX analysis of gold-enriched SPMN materials.

EDX analysis shows that the main composition of the material is iron, oxygen and gold. The presence of iron and oxygen confirms that the material is an iron oxide and the presence of gold confirms the adsorption of gold species by the SPMNs. As illustrated in *Figure 38*, we propose that the gold adsorbed was coated as an outer layer onto the surface of the SPMNs. However, we still need to investigate this hypothesis. Since the SPMNs before the gold adsorption was approximately 10 nm in diameter and from the result of the pseudo-trigonal shaped particles obtained (*Figure 37*), we can conclude that the gold coating onto the SPMNs is approximately 2 – 3 nm in width. This is still the topic of much research and worth looking at further.

Section A4 – The extent of iron dissolution

The aqueous solutions can play an important role on the dissolution of iron oxide materials.[42] Magnetite usually dissolves faster than other iron oxides due to both Fe(II) and Fe(III) content in their crystal structure. Experiments were therefore designed to investigate the effect of various aqueous acidic solution conditions on the iron dissolution of the magnetite based nanoparticle materials. The amount of resin degradation over time caused by magnetite that dissolved as a result of the acidic content of the aqueous solutions in which the sorption batch experiments have been performed, were investigated. In this regard, the iron dissolution (as mass %) for magnetite (Fe_3O_4), silica-coated SPMNs (FeSi) and the amine-functionalized magnetite nanomaterials (FeSiAPTS and FeSiED), were studied to determine the robustness of these resin materials. A constant mass of the nano-sized materials were contacted for a certain amount of time with hydrochloric acid solutions consisting of concentrations ranging from 0.5 M – 3.0 M HCl and in the pH range 3 – 6. The supernatant were collected *via* magnetic sedimentation by applying an external magnetic field. The amount of iron in solution was detected by ICP-AES and using mass balance equations the amount of iron dissolution could be calculated. The results of these findings are given in *Figure 39* and a visual characterization showing the amount of iron dissolution (corresponding to this result) of only the Fe_3O_4 nanoparticles can be seen in *Scheme 14*.
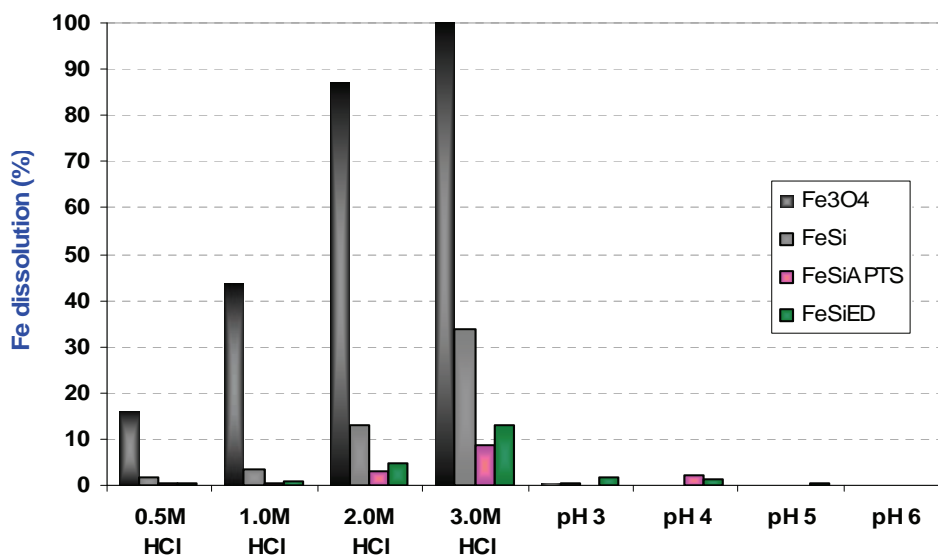
Figure 39. The amount of iron dissolution as a function of pH of the aqueous acidic solutions. Experimental conditions – mass material used: 50 mg; Total metal aqueous phase: 15 mL; Contact time: 150 minutes; Temperature: 21 ± 1ºC.

As can be seen in *Figure 39* and *Scheme 14*, there is an increase in iron dissolution as one proceeds from 0.5 M HCl to 3.0 M HCl. As expected, the highest percentage dissolution was found for bare magnetite as compared to the relatively low dissolution of the silica-coated amine-functionalized magnetite nanocomposite materials. In particular, for bare magnetite, *ca* 17 % dissolution occurred for the 0.5 M HCl solution experiments and 100 % dissolution was found for the 3.0 M HCl solution experiments. As indicated by the results obtained for the silica-coated magnetite nanoparticles, the silica layer indeed provides a protective layer against acidic conditions, with less than 2 % dissolution in the 0.5 M HCl solution experiments. However, a similar trend is observed, with increasing dissolution as the molarity of the solutions increases. To illustrate the protective mechanism that the silica layer offers, for the 3.0 M HCl solution experiment about 34 % dissolution was found to occur as compared to the 100 % dissolution for bare magnetite. Moreover, it was found that upon functionalizing the silica coated materials, the resistance against acidic conditions improved even more. Also, the iron dissolution of the materials was investigated in pH 3 – 6 ranges. In these studies, the amount of dissolution was almost negligible as shown in *Figure 39*.

| 0.5 M HCl | 1.0 M HCl | 2.0 M HCl | 3.0 M HCl | pH 3 | pH 4 | pH 5 | pH 6 |
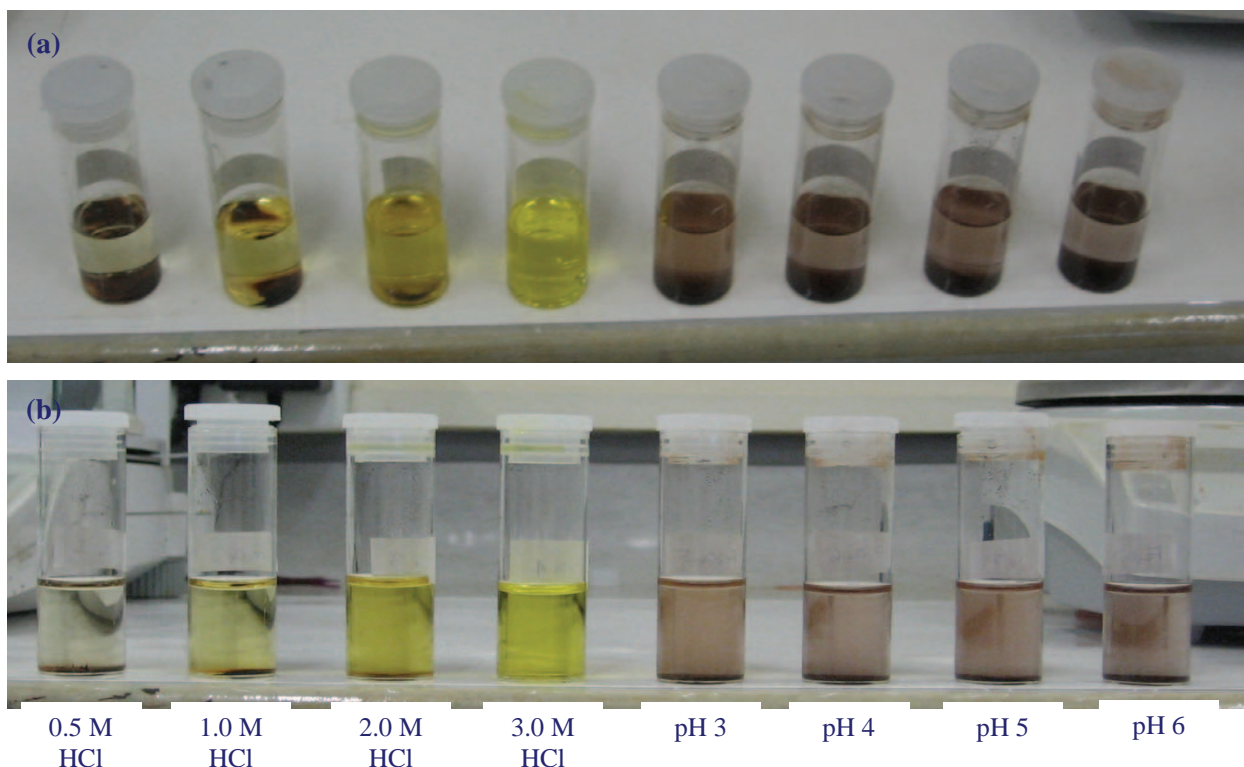
Scheme 14. Visual illustration of the amount of iron dissolution for Fe₃O₄ nanoparticles in various acidic solutions corresponding to result in Fig. 39; (a) top view and (b) side view.